Optical spectroscopy of cooperative phenomena and their symmetries in solids

DISSERTATION

Presented in Partial Fulfillment of the Requirements for the Degree Doctor of Philosophy in the Graduate School of The Ohio State University

By

Thuc Tan Mai, BSc

Graduate Program in Physics

The Ohio State University

2019

Dissertation Committee:

Prof. Rolando Valdés Aguilar, Advisor

Prof. P. Chris Hammel

Prof. Nandini Trivedi

Prof. Douglass Schumacher

ABSTRACT

In crystalline materials, the symmetry of the crystal lattice imposes strict conditions on the observable properties of the material. These symmetry restricted conditions can be, in turn, probed by light via the electromagnetic interaction. Studying the electromagnetic excitations in solids can reveal many fundamental properties of these systems. A quick introduction and guide to symmetry in solids will be given, with an emphasis on how it can be used to interpret spectroscopic measurements. The measurement techniques used will also be described. Time domain Terahertz spectroscopy (TDTS) is the main technique used in this dissertation. Important experimental considerations pertaining to the construction of the THz spectrometer will be given.

In the multiferroic $Sr_2FeSi_2O_7$, we found multiple excitations in the few meV energy scale (THz), in the material's paramagnetic phase. Measurements with varying temperature and magnetic field revealed that these excitations are both electric and magnetic dipole active. By considering the ground state of the Fe^{2+} magnetic ion in $Sr_2FeSi_2O_7$, we concluded that our observation is coming from the spin-orbital coupled states of the ion. This realization demonstrated that spin-orbit coupling plays a crucial role in these exotic materials. Interestingly, these spin-orbital THz excitations persist into the magnetically ordered phase. The single-ion picture of the paramagnetic phase needs to be expanded theoretically to explain our observations.

$CaFe_2O_4$ orders antiferromagnetically below ~ 200 K. Two co-existing magnetic structures (A and B phase) have been measured previously by neutron diffraction. The anti-phase boundaries between these two phases have been proposed to be the cause of the quantized magnetic excitations (magnons) measured by an inelastic neutron scattering study. We

measured two antiferromagnetic resonances (magnons) with TDTS. Our observation can be explained by the orthorhombic crystal anisotropy of $CaFe_2O_4$. Mean field classical spin wave analysis confirmed that indeed the magnon modes come from the low symmetry of the crystal. These two modes were found to have the same temperature dependence of only the magnetic B phase. We did not observe the hierachy of quantized magnon modes as previously reported. However, our measurements offered a hint of another magnon mode that show temperature dependence similar to the other magnetic structure, A phase.

In the last study, we demonstrated the lattice symmetry breaking effects on the Raman phonon spectrum of α-$RuCl_3$ at room temperature. The Raman spectrum shows multiple pairs of phonon peaks with approximately 2 cm^{-2} (0.248 meV or $\approx$ 60 GHz) apart. This observation can be explained by the symmetry lowering effect when going from a perfect honeycomb layer (D_{3d} point group symmetry), to the monoclinic bulk crystal (C_{2h}). Furthermore, because of the honeycomb layer structure, this material is a host candidate for the long-sought-after Kitaev quantum spin liquid. Following previous experimental and theoretical studies with Raman spectroscopy on α-$RuCl_3$, we concluded from our data that the scattering continuum is magnetic in origin, with little to no quasi-elastic scattering contribution.

To my loving parents

Acknowledgments

Vita

May, 2011 .... BSc, Syracuse University

Publications

T. T. Mai, C. Svoboda, M. T. Warren, T.-H. Jang, J. Brangham, Y. H. Jeong, S.-W. Cheong, and R. Valdés Aguilar, "Terahertz spin-orbital excitations in the paramagnetic state of multiferroic $Sr_2FeSi_2O_7$", Phys. Rev. B 94, 224416 (2016)

A. M. Potts, T. T. Mai, M. T. Warren, and R. Valdés Aguilar, "Corrective re-gridding techniques for non-uniform sampling in time-domain terahertz spectroscopy", J. Opt. Soc. Am. B 36, 1037-1043 (2019)

Evan V. Jasper, T.T. Mai, M.W. Warren, R.K. Smith, D.M. Heligman, E. McCormick, Y.S. Ou, M. Sheffield, R. Valdés Aguilar, "Broadband Circular Polarization Time-Domain Terahertz Spectroscopy", arXiv:1811.06037

Daniel M. Heligman, A.M. Potts, N. Crescimanno, M.T. Warren, E.V. Jasper, T.T. Mai, R. Valdés Aguilar, "Size and Periodicity Effects on Terahertz Properties of Gammadion Metamaterials" arXiv:1811.06041

Amber McCreary, Robert McMichael, Jeffrey R. Simpson, Jason Douglas, Nicholas Butch, Thuc Mai, Cindi Dennis, Rolando Valdés Aguilar, Angela R. Hight Walker, "Validation of a Spin Wave in 2-Dimensional Antiferromagnetic $FePS_3$ via Magneto-Raman Spectroscopy", *Manuscript In Preparation*

Thuc T. Mai, A. McCreary, P. Lampen-Kelley, N. Butch, J.R. Simpson, S. Nagler, D. Mandrus, A.R. Hight Walker, and R. Valdés Aguilar, "Symmetry breaking effect on the Raman phonon spectra of α-$RuCl_3$", *Manuscript In Preparation*

Fields of Study

Major Field: Physics

Table of Contents

List of Figures

List of Tables

Chapter 1
INTRODUCTION

1.1 General concepts

What is spectroscopy?

First, we can define spectroscopy as the study of the interaction between light and matter. The rainbow of colors that human can see is called the visible spectrum. It turns out that the human eyes are spectrometers. We are engaging in spectroscopic measurements when we are using our eyes to perceive the world around us. For example, while looking at a red box, a person's eyes would be detecting the electromagnetic (EM) waves coming from the box, with frequencies corresponding to the color red. It is important to point out that in order to see, some light source has to be present. Human are not able to see any color (in fact at all) in darkness. In the presence of daylight or adequate indoor lighting, we can discern if a box is red, or blue, or any color of the rainbow.

At this point, one might ask: why does the red paint looks red? After reflecting off the surface of a painted objects, the light spectrum that enters the eyes contains mostly EM waves corresponding to red. One might note that the light source illuminating the painted object might appear to be colorless, or at least not purely red. We automatically make these observations in our daily lives. The purpose can be as primal as noticing a dangerously hot surface, to as utilitarian as color coding your luggage. Furthermore, systematically comparing the EM spectrum coming directly from the light source and the spectrum reflected off the painted surface can provide important information about the

chemical makeup of the paint.

At this point, two important components to spectroscopy should stand out, a spectrometer (the human eyes) and a light source (the sun). With these two components, we go about our daily lives subjecting everything we encounter under a close study, albeit without much concious effort. As you will find out in the rest of this thesis, I will give a summary of important findings from my spectroscopic study of a variety of solids. Although the spectrometers and light sources that I have used are designed for colors that human eyes cannot see, the same principles still apply.
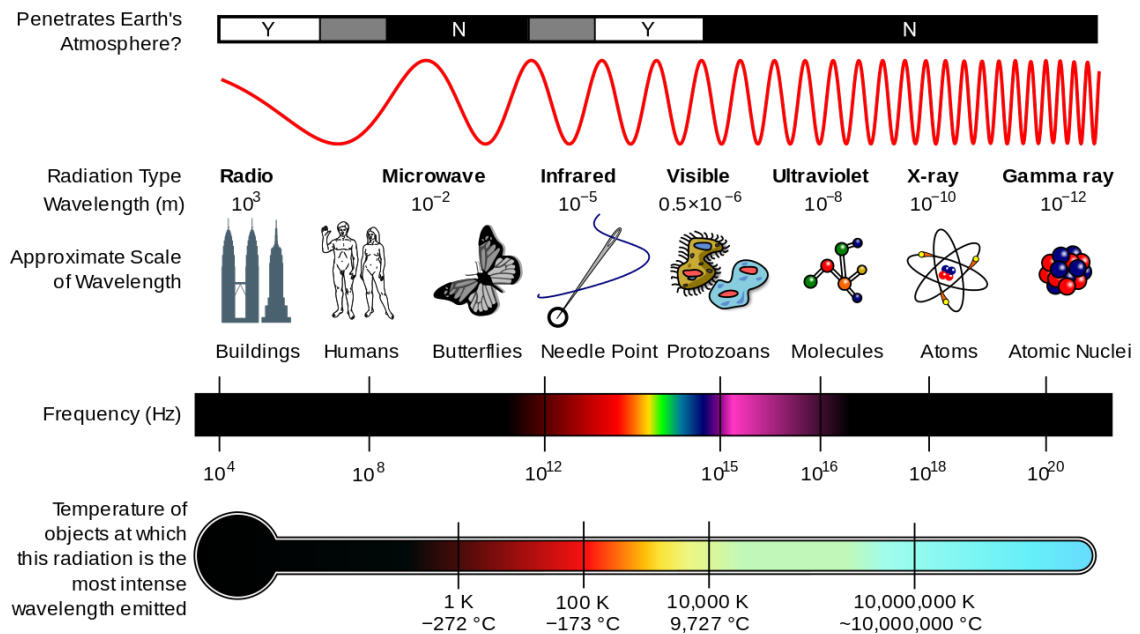
Figure 1.1: **Electromagnetic spectrum**[1]. One of the pillars in modern physics is the discovery of the speed of light. This massless particle, that also behaves like a wave, has a constant speed in vaccuum, c. This number has recently been defined to be a standard so that other measurement units (meter, second, etc.) are based on it. Given the wave nature of light, they wavelength can vary infinitely from smaller than the size of an atom to larger than the height of a skyscraper. The human eye operates at a much narrower wavelength range in between. Many interesting phenomena in physics happen beyond what the human eyes can perceive.

Some history

In the 1600s, Sir Issac Newton used a glass prism to make the observation that sunlight is made up of many color. Then in the 1800s, William Herschel extended this idea, establishing that there exists "colors" we cannot see. At the beginning of the 20th century, J.K. Maxwell showed us that light is an electromagnetic wave. Max Planck and Einstein took it a step further and proposed an idea that there is a fundamental unit in a beam of light, a photon, each carries a discrete amount of energy, which is proportional to its frequency.

Our modern understanding of light have been well tested. We know that the speed of light in vacuum is a fundamental constant of nature. The basic equation of waves relating its frequency f (how fast the wave goes up and down) to its wavelength λ (distance from crest to crest) is: $\lambda f = c$. c is the speed of light. It stands to reason that the wavelength and frequency, λ and f, tell us the same information in vacuum. The problem becomes more interesting when light enter a medium. That is where spectroscopy comes in.

To go back to the discovery of Max Planck, the quantum of energy that light carry is directly proportional to its frequency f (the proportionality constant is named after Max Planck). The law of conservation of energy tells us that f should not change when light goes from vacuum to a medium. Hence, studying the spectrum should reveal to us what frequency of light is missing due to the medium. In this simplified picture, there is a phenomena inside the medium that absorb certain frequency of light. The job of an optical spectroscopist is to exploit the interaction between light and matter to probe such properties matter.

1.2 Spectroscopy in condensed matter physics

Condensed matter (CM) is a sub-discipline in physics. A short history lesson about condensed matter physics can be found in the Jan 2019 publication of Physics Today[9]. This branch of physics focuses on the many emergent phases of matter that exists in solid.

Why do we do this? Many phenomena in CM physics of great interest can be studied with optical spectroscopy 1.2. The drive can easily come from the search for a fundamental
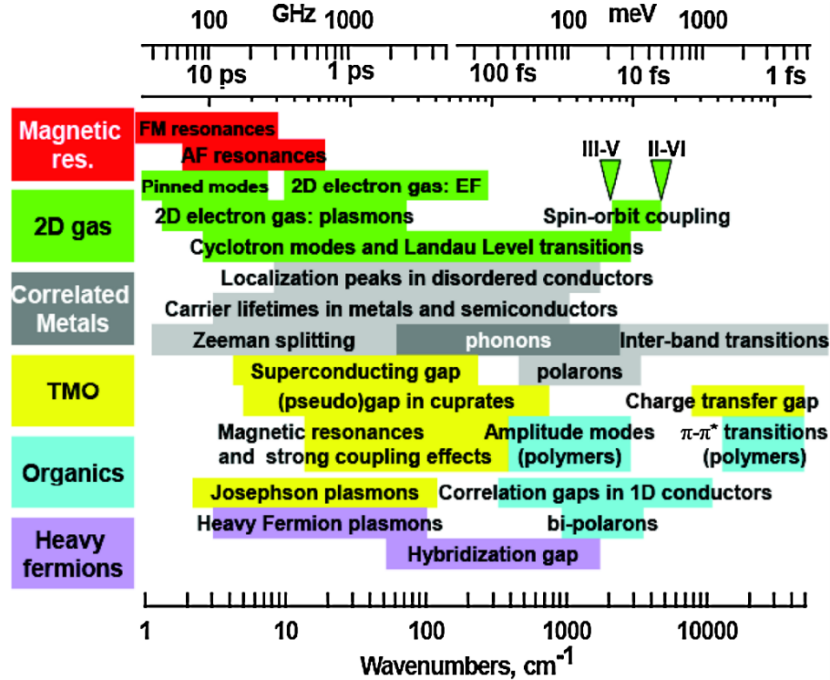
Figure 1.2: **Some interesting phenomena in the infrared and far-infrared spectrum in condensed matter physics**[2]. From the more exotic high Tc superconductor's Josephson plasmons to more common carrier lifetimes in metals and semiconductors, infrared and far-infrared (THz) spectroscopy is the perfect tool to study these phenomena in solids.

physical law to a more application-centric perspective, often times both. To narrow down the scope, the focus of my Ph.D. research has been on phenomena that has its energy characteristic in the far infrared. Within this energy range, magnetic and lattice vibration resonances are my primary focus. I will attempt to give a general introduction to these phenomena. Detailed description can be found in most condensed matter/solid states text book (like this one by Ashcroft and Mermin [10]).

Resonances in crystalline solids

Examples of resonant phenomena can be seen in our daily lives. It can be as simple as a guitar string producing a "pure" sound, or the near constant swing of a clock pendulum. Anyone who has pushed a child on a swing set would recognize that there is a "right" time to push. In physics the model concept for resonances is a mass on a spring. As one

4

displace the mass from its equilibrium position (if placed in this position, the mass and spring would remain there forever), the spring force (related to how stiff it is) would pull or push the mass back to it's equilibrium. It turns out that this simple concept is the basis to understand many physical phenomena. We can almost always relate resonances to something that resembles a spring constant k (stiffness of the spring) and a mass m. The natural frequency (resonant frequency) is proportional to the square root of k/m.

For example, one can think of a solid as many atoms connected by springs. The end result is that there are natural frequencies at which this model solid would vibrate at. If we change the atoms to a heavier type, we should expect the resonant frequencies to become lower. In a real solid, the situation is much more complicated. As different atoms have different masses and sizes, the "springs" that hold them together could also change. However, this simple and intuitive concept is a great place to start when trying to make sense of spectroscopic data. What I've mentioned is the simplest model of a phonon. Phonons are resonant or *normal modes* of vibration in a crystal.

What is a crystal? The basic definition is the regular, well-defined arrangement of atoms. A perfect crystal is made up of perfectly stacked, identical *unit cells*, each containing a few to several hundreds of atoms. The unit cells form a periodic lattice, and stacked in such a way that it would fill in all the space. Although not a perfect analogy, one can think of the unit cells as boxes of identical shape, and the lattice is the periodic pattern that you can stack them. It turns out that there are only a few shapes that would fit together perfectly so that there would be no gap. A good example of a shape that would leave gaps is the pentagram in 2 dimensions. Although finding all the shapes that would fit our criteria is an interesting discussion, the details are outside the scope of this thesis. In 3 dimensions, there are only 14 lattice types. These Bravais Lattices define the shapes of the unit cells and are the basic building patterns of crystals.

A phonon is considered a cooperative phenomenon, where all the atoms in the crystalline lattice vibrate together. Phonons are often studied as a way to probe the type of crystalline lattice, or any changes to the lattice that might occur as a function of temperature. There are many other cooperative phenomena in solids (some are seen in fig. 1.2). Magnon is

5

another type that's associated with magnetism. If we imagine each atom on a lattice having a small magnetic moment (tiny magnet), and the moments have a way to talk to each other like the chemical bonds between atoms, then a small uniform precession is the magnon (in contrast to the phononic vibration). Studying these phenomena is a great way to probe the fundamental properties of condensed matter systems.

Some spectroscopic techniques to probe phonons and magnons

Fortunately, the electromagnetic force is a fundamental one. Barring the more elusive and exotic dark matter, ordinary matter interacts with each other via these fundamental forces. This means that spectroscopy can be performed on any ordinary matter. The experiment can be a simple one: shine light onto solid and measure light scattered off of solid. Unfortunately, there are many phenomena that would affect the electromagnetic spectrum. There is a trade-off between how simple the experiment is and how difficult it is to interpret the result. As experimentalists, we can devise more complicated schemes to eliminate possible causes to the result.

The simplest experiment can be done with a light source and a spectrometer. In the infrared regime, Fourier Transform Infrared Spectroscopy (FTIR) is a widely used technique. Here, a sample is placed between a heat lamp (not unlike an incandescent light bulb) and an interferometric spectrometer (a special technique that allows the measurement of a spectrum from near visible to "far infrared" light). Time-domain Terahertz spectroscopy is similar in experimental simplicity to FTIR. However, the detection of THz frequency spectrum (0.1-3 THz) is easier and less costly than with an FTIR. Our group at Ohio State University has the experimental expertise in THz spectroscopy. Raman spectroscopy is typically a complemental technique to FTIR (and THz) in determining the phonon spectrum of a material. Some details will be given in the next section.

Chapter 2
BASIC THEORY OF LIGHT-MATTER INTERACTION IN SOLIDS

What we are interested in studying is how an electromagnetic(EM) wave interacts with solids. The macroscopic treatment of Maxwell's equation in a medium can be seen in most Electromagnetism textbooks. I will highlight some important points as a guide to later discussions. Just to note, everything is written in Gaussian unit.

2.1 Electromagnetic waves in solids

One of the great discoveries in physics is the description of light as an electromagnetic wave by James Clerk Maxwell. In this section, a brief introduction to how light behave in solids will be given. The units are in CGS and no assumption about μ is made. This introduction is adequate to showcase the type of information that can be extracted from a spectroscopic measurement. Starting with the plane wave solution to Maxwell's equations in vacuum:

$$\mathbf{E}(\mathbf{r}, t) = \mathbf{E_0} e^{-i(\mathbf{k_0} \cdot \mathbf{r} - \omega t)}$$

$$\mathbf{B}(\mathbf{r}, t) = \mathbf{B_0} e^{-i(\mathbf{k_0} \cdot \mathbf{r} - \omega t)} \tag{2.1}$$

$$\omega \mathbf{B_0} = \mathbf{k_0} \times \mathbf{E_0}$$

Here, $\mathbf{E}$ and $\mathbf{B}$ are the electric and magnetic field; $\mathbf{r}$ and t are position and time coordinate; $k_0 = 2\pi/\lambda$ and $\omega = 2\pi/f$ are the wave vector and angular frequency. $\mathbf{E_0}$ and $\mathbf{B_0}$ are

vectors. These vectors are transversed to the wave vector for plane waves. One can define the unit vector of the electric field $\mathbf{e}$:

$$\mathbf{E_0} = E_0\mathbf{e} = E_0 \begin{bmatrix} \tilde{e}_i \\ \tilde{e}_j \\ \tilde{e}_k \end{bmatrix}$$

$$\mathbf{k_0} \cdot \mathbf{e} = 0$$

(2.2)

The tilde sign represents complex quantities. At finite frequency, we expect the properties of the medium to be complex. In a medium, where the material can respond to the changing electric and magnetic field of light, it is useful to have Maxwell's equation in this form:

$$\nabla \cdot \mathbf{D} = 4\pi\rho^{free}$$
$$\nabla \times \mathbf{E} = -\frac{1}{c}\frac{\partial \mathbf{B}}{\partial t}$$
$$\nabla \cdot \mathbf{B} = 0$$
$$\nabla \times \mathbf{H} = \frac{1}{c}(\frac{\partial \mathbf{D}}{\partial t} + 4\pi\mathbf{J}^{free})$$

(2.3)

Where $\mathbf{D}$ and $\mathbf{H}$ are the auxiliary fields; ρ^{free} and $\mathbf{J}^{free}$ are the free charge and current density. From this macroscopic point of view, the quantities of interest in our measurements are ε and μ, the dielectric function and magnetic permeability. They represent the response functions of the material under the the influence of EM fields. These response functions are hidden in the auxiliary fields, within the linear approximation:

$$\mathbf{D} = \mathbf{E} + 4\pi\mathbf{P} = \varepsilon\mathbf{E}$$
$$\mathbf{H} = \mathbf{B} - 4\pi\mathbf{M} = \frac{1}{\mu}\mathbf{B}$$

(2.4)

Here, the macroscopic electric polarization $\mathbf{P}$ and magnetization $\mathbf{M}$ can depend on any power of $\mathbf{E}$ *and* $\mathbf{B}$. We shall only focus on the linear response in this analysis. Many important non-linear effects are described in nonlinear optics textbooks such as one by

8

Boyd [11]. By substituting eq. 2.1 into eq. 2.3 and 2.4, one can derive the following useful relationships:

$$\tilde{n} = n_1 + in_2$$
$$\tilde{\varepsilon} = \varepsilon_1 + i\varepsilon_2 = \frac{\tilde{n}^2}{\tilde{\mu}} \qquad (2.5)$$

Here, n_1 and n_2 (ε_1 and ε_2) are related in a fundamental way via the Kramers-Kronig relation. This relation is a direct consequence of causality and it relates the real to the imaginary part of these optical "constants" in a medium [12]. In experiments where the detector can only detect the intensity of light, Kramers-Kronig analysis can be useful in determining the real and imaginary part of these properties. In measurements such as Terahertz time-domain spectroscopy, the electric field of light can be determined as a function of time. We do not need to use Kramers-Kronig as the data preserve the phase information. A brief guide to our analysis method can be found in later chapters.

One should note that $\tilde{\varepsilon}$ is not only a complex quantity, but can also be a tensor. In an *isotropic* medium, one expect $|\tilde{\varepsilon}|$ to remain the same as we measure different orientation of the medium. This is typically carried out by physically rotating the subject while keeping the instrument unchanged, or by changing the polarization of light. Within the linear response regime, the rank 2 tensor representing $\tilde{\varepsilon}$ is a constant complex number times the identity matrix for an *isotropic* crystal. The situation is much more interesting in an *anisotropic* medium. A rank 2 response tensor, in this case $\tilde{\varepsilon}$, is a matrix of this form:

$$\tilde{\varepsilon} = \begin{bmatrix} \tilde{\varepsilon}_{xx} & \tilde{\varepsilon}_{xy} & \tilde{\varepsilon}_{xz} \\ \tilde{\varepsilon}_{yx} & \tilde{\varepsilon}_{yy} & \tilde{\varepsilon}_{yz} \\ \tilde{\varepsilon}_{zx} & \tilde{\varepsilon}_{zy} & \tilde{\varepsilon}_{zz} \end{bmatrix} \qquad (2.6)$$

2.2 Experimental details

In this section, I will give a brief description of the techniques used in my measurements.

2.2.1 Time Domain Terahertz Spectroscopy (TDTS)

Most commercial and home-built TDTS cover the frequency range of about 100 GHz to 3 THz (or 0.414 meV to 12.417 meV). This energy range makes TDTS suitable to study low energy phenomena in solids such as plasmon resonances, antiferromagnetic resonances, superconducting pairing energy, etc. (Fig. 1.2) This technique offer one of the more unique ability that's available to spectroscopy. The coherent aspect of the light source combines with the short pulses (broad bandwidth) and the time-domain sampling to automatically produce magnitude and phase information of these phenomena.

This technique is relatively new. In the 1980's, David Auston demonstrated the ability of a photoconductive switch to generate broadband radiation when coupled with an ultrafast laser [13, 14]. Through various optimizations, the Auston switch became an ideal source and detector for THz spectroscopy [15]. Presently, there exists other techniques that uses non-linear optics to generate and detect THz radiation in the time domain [16]. The main goal of these non-linear sources and detectors is to widen the bandwidth of the radiation, some upward to more than 10 THz. One of the latest development in the technique is the use of the inverse-hall effect in the so called "spintronic emitters" [17].

In general, a TDTS system is made up of an ultrafast laser, an emitter, a detector, a time-delay mechanism, optical components for steering the radiation and electronics for collecting the data. The details of how to set up your own system are detailed in numerous PhD thesis. As I had to build up these systems from scratch, the most useful resource that I found is a thesis by Luke Bilbro from Johns Hopkins University [18]. In addition, the experimental philosophy that I followed when designing and aligning these spectrometers will be discussed below.

There is a fundamental assumption used in TDTS: each THz pulse created are identical to the others. For this assumption to hold, we need to use a stable infrared laser and low-noise acquisition instruments. What we've found in our lab is that laser stability is the biggest issue. A commercial 800nm Ti:Sapphire ultrafast laser can stay nearly 99% stable for many hours. However, ambient condition may change in the course of an hour, especially

if the environmental control is not functioning correctly. It is absolutely crucial to have a well regulated room, or a sealed laser. In any case, an imperfect room might be adequate, given that the drift in ambient condition is slow, $\sim$ hours. Therefore, it is important to monitor and anticipate environmental drifts when performing spectroscopic measurements.

A TDTS system might look like Figure 2.1 [4, 19]. Here, the radiation generated from the emitter, efficiently coupled to free space via a Silicon hyper-hemispherical lens, travels to the Silicon lens on the detector via the off-axis parabolic (OAP) mirrors. The emitter and detector that we use are photoconductive antennas with identical geometry (Fig. 2.2).
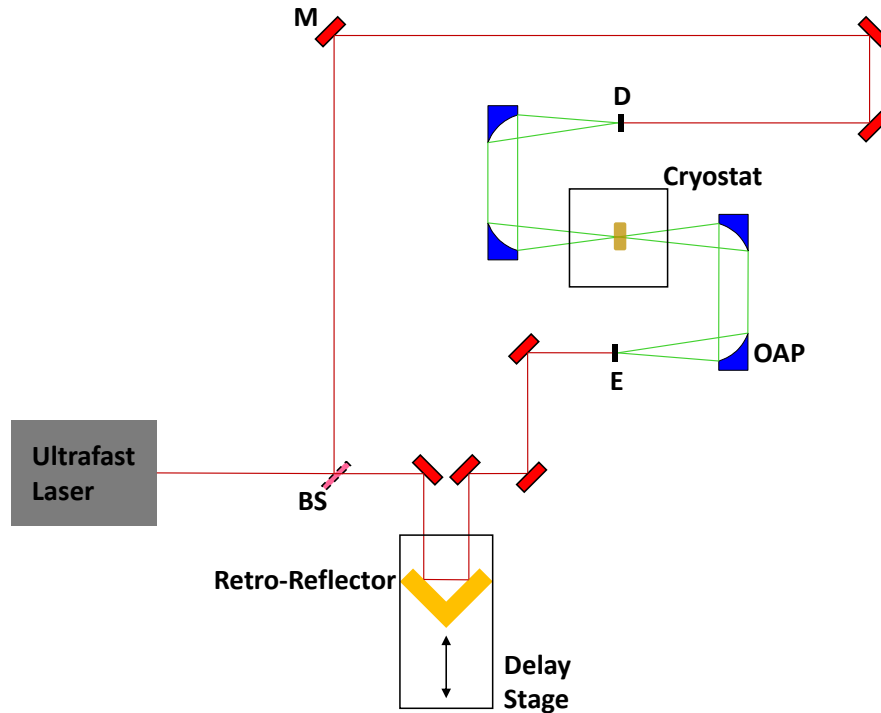
Figure 2.1: **TDTS Schematics**. M - Mirror; BS - Beam Splitter; D/E - Detector/Emitter; OAP - Off-axis Parabolic (mirrors); The sample is in the center of the cryostat. The infrared (IR) beam is represented by red lines, while the larger THz beam is outlined by green. The path length of the IR beam is not to scale while the path length of the THz beam is equal to 8f, were f is the effective focal length of the OAP mirrors. The arrangement of the OAP mirrors is specifically design to minimize aberration [3, 4].
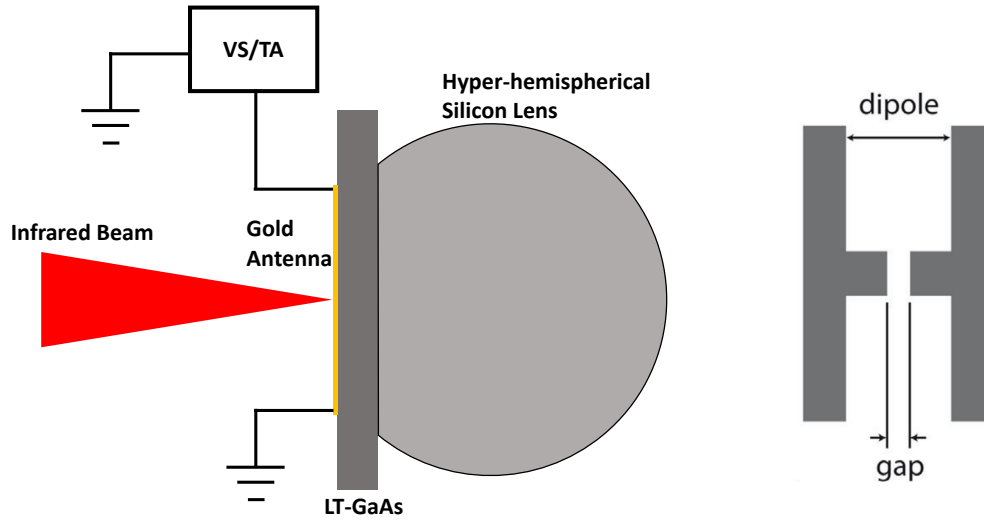
Figure 2.2: **Schematics of Emitter/Detector**. The ultrafast beam is focused onto a small gap in the antenna structure. The metallic antenna structure is typically made of gold, on top of a photoconductive material (Low Temperature grown GaAs). In our laboratory, the Auston switches were purchased from Menlo Systems. The gap is $5\mu m$, while the striplines (labeled dipole) are $20\mu m$ apart. The striplines of the emitter are connected to a voltage source (VS), and for the detector, a transimpedance amplifier (TA). The Si lenses also serve as an index-matching material to efficiently couple THz radiation between LT-GaAs and air.

To generate THz radiation, an ultrafast infrared pulse (800 nm) is incident upon a small gap ($\sim 10\mu m$) between two metallic electrodes. Inside the gap is a photoconductive material with short recombination time ($\sim$ 100 fs). The infrared pulse turns the photoconductive material on, making them temporarily conductive. The duration of the infrared pulse is much shorter compared to the photoexcited carriers' lifetime. By having a constant voltage across the electrode, we have a situation that's equivalent to the turning on an off of an electrical circuit on a sub picosecond time scale. The pulse of current that runs through the emitter creates the THz pulse.

In principle, the detector is an identical device to the emitter. Instead of a constant

voltage from an external source, the voltage across the electrodes in the detector comes from the radiation that it's trying to detect. A current meter is connected to the metal electrodes as a mean to detect the current driven by the radiation itself. By changing when the detector get turned "on" by the infrared pulse, the electric field of many identical THz pulses can be measured. Once again, this measurement scheme only works if the fundamental assumption holds.

If you are keeping track, the detector should be "on" for a duration that's similar to the duration of the THz pulse. The discussion about how and why the detection (and also generation) process works can be found in other thesis (like the one here [18]). The reasons can be summarized as followed. The detected signal is a convolution of the response function of the detector and the THz pulse. Although the time scales are similar, the peak responsiveness of the detector is much shorter than the THz pulse. As a consequence, the temporal resolution of the detected signal is limited by the rise and fall rate of the detector's response function.

Experimental considerations in building a TDTS

In building up a TDTS, one of the biggest challenge is alignment. The main reason is that THz radiation is low energy. In addition, the intensity generated by the photoconductive antennas are also low, $\sim \mu W/cm^2$. For those reasons, a simple piece of paper and/or an IR-Scope cannot be used. Detectors for THz or far-infrared frequencies are fairly sophisticated and do not lend themselves to the quick and mobile nature of alignment. Fortunately, the advantage of low energy EM waves is the long wavelength of THz radiation, it is much more forgiving to thermal drift of the OAP mirrors (relative to the silver or dielectric mirrors used for $800nm$ light). Hence, once the THz optics are well-aligned, it will remain so for almost indefinitely (or longer than the duration of a PhD).

The general scheme of alignment that I've found successful is to fix the position of the FRUs (or field-replaceable units) and the OAP mirrors with machine precision, 1 "mil" or $\sim 25\mu m$, and use two FRUs to control the position of the emitter and detector. One should note that $25\mu m$ is smaller compare to the wavelength of 1 THz, $\sim 300\mu m$. The strategy

is to use the FRU's micro-positioners (with $\sim 1\mu m$ accuracy) to correct for the error from machining. Alignment of the IR beams is detailed in this thesis[18]. The method to align the THz beam is also mentioned in the same thesis (although the degrees of freedom are much larger).

The last piece of this puzzle is the alignment of the hyper-hemispherical Silicon lenses. I find that due to the long wavelength nature of THz, it is adequate to "estimate" their correct positions for the initial state. In this initial state, one should be able to measure a noisy THz pulse (given the correct planning of path lengths, IR beam alignment, and machining accuracy). If the planning, machining, and alignment has been done correctly, the only necessary adjustments are in the position of the Si lenses. By monitoring the peak signal of the measured THz pulse while going through iterations of adjustment in the x-positions of the lenses and then y-positions, an optimal pulse can be obtained. It is paramount to have a well designed data acquisition interface, capable of quickly moving the mechanical delay stage and visible signal read-out in real time.

Once the signal from the peak of the THz electric field pulse no longer increase with Si lenses alignment, the system should be close to well-aligned. Monitoring the *usable bandwidth* of the THz pulse is a good way to check for this. With emitter and detector made from LT-GaAs, this bandwidth should be from 0.1 to 2.5 THz. We determine these numbers by taking consecutive measurements of the freely propagating THz pulse, find the average time-domain signal, Fourier transform all the measurements and the average, then take the ratios of each measured spectrum to the average spectrum (Figure 2.3). This method will show where the signal-to-noise ratio (SNR) becomes too large for us to make a repeatable observation. Our criteria is where the amplitude ratio diverges more than 2% from 1.

Minor adjustments can be made in the position of the emitter and detector along the beam path. One can use the same approach as the alignment of the Si lenses. It should be pointed out that the spectroscopic measurements that we perform involve a low temperature cryostat. These instruments have multiple windows for light to travel through. The addition of these windows can reduce the *usable bandwidth* significantly. I found that re-adjustment
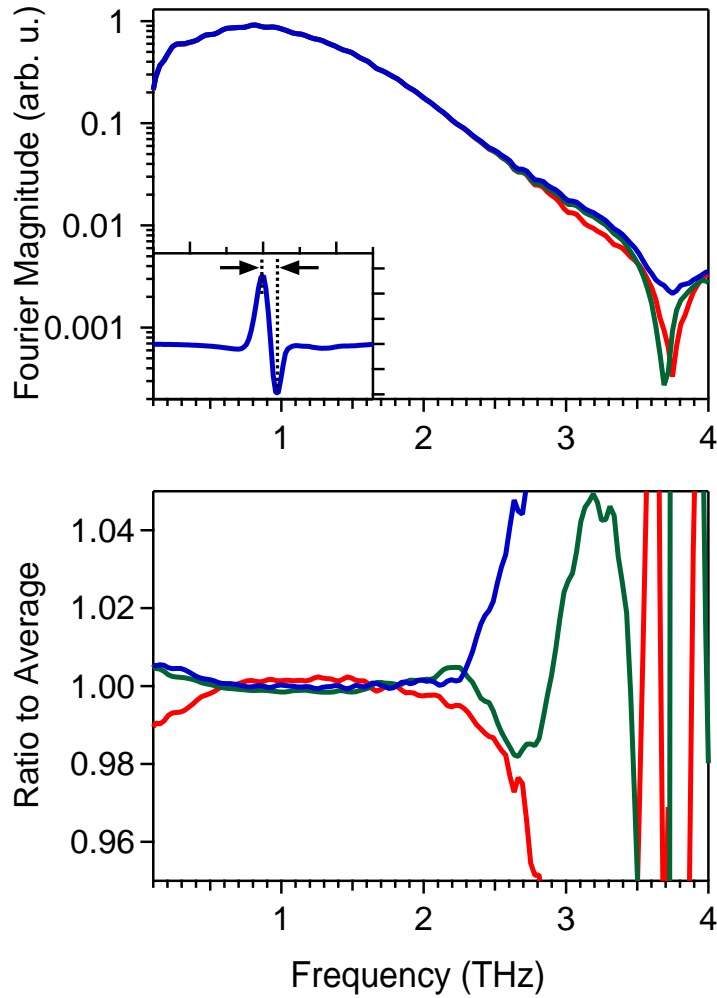
Figure 2.3: **Usable THz bandwidth**. With photoconductive antennas made from LT-GaAs, we get a pulse width of $\approx 0.4ps$ (inset). The spectrum extends from 0.1 THz to nearly 4 THz (top graph). However, the ratio of the individual spectrum to the average (time-domain average) spectrum shows that the signal to noise ratio becomes too low above $\sim$2.5 THz (bottom graph). The bottom graph is a measure of our repeatable bandwidth.

of the Si lenses and emitter/detector positions along the beam path is necessary to achieve

optimal bandwidth. In commercially available cryostats, the windows are typically made

out of amorphous glass (SiO_2). The lowest optical phonon in glass attenuates our signal,

reducing the upper limit of our bandwidth to less than 2 THz.

I found that changing the glass windows to films ($133\mu m$ thick) of Kapton eliminates

the phonon attenuation problem while preserving the integrity of the vacuum jacket of the

cryostat. There is a small problem of water diffusion across the thin Kapton films, making it difficult to achieve high vacuum. Water vapor also poses a problem to THz spectroscopy as there are a plethora of resonances in water molecule in the THz regime. Fortunately, water vapor is in a TDTS system by constantly flowing Nitrogen gas into a semi-closed box that encloses the system.

Useful equations to extract optical properties

By placing a sample in the THz beam path, we can measure the transmitted THz electric field. Fourier Transforming the transmitted THz pulse and dividing it by the Fourier Transform of a reference pulse (no sample), we can obtain the transmission function via eq. 2.7. An example is given (see Fig. 2.4, 2.5). The Kapton films exhibit the Fabry-Perot effect, which happens when the multiple reflections inside the film constructively and destructively interfere. However, the effect exists in both sample and reference pulses and get divided out in the frequency domain.
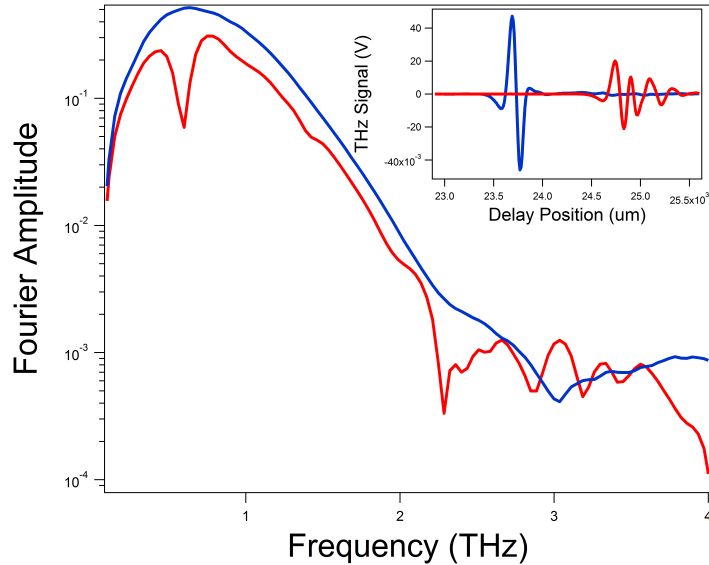
Figure 2.4: **Example of measured sample and reference spectra**. The red curves are the Fourier spectrum (magnitude only) and the measured time domain pulse (inset) of the transmitted electric field through $Sr_2FeSi_2O_7$. The blue curves are the references (no sample). By dividing the two spectra, as in eq. 2.7, we can obtain the complex transmission function of this material.

16
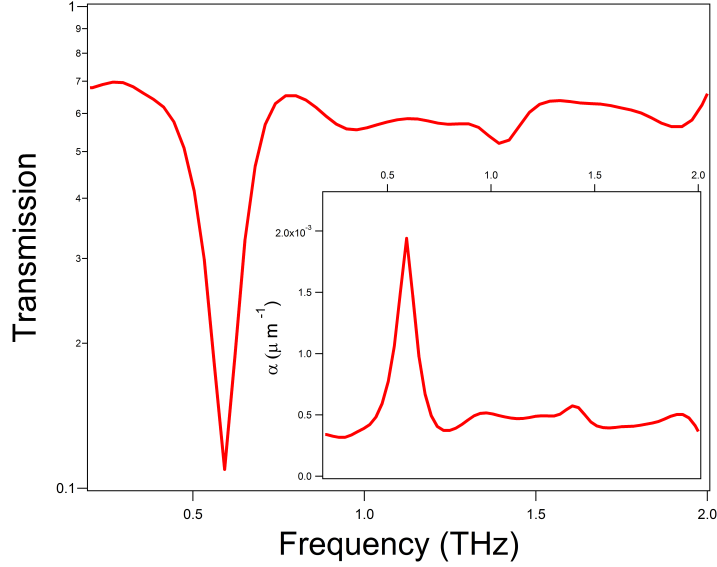
Figure 2.5: **Example of transmission (magnitude) and the absorption coefficient** α. The transmission is obtained from fig. 2.4. Here we define the absorption coefficient α as minus the natural log of the magnitude of the transmission function, divided by the sample's thickness.

This transmission function can be model by the shape of the sample. The most common samples that we studied are either a simple slab or a thin film on a thicker substrate. In either case, they depend on the Fresnel equations [12]. Details of such analysis can be found elsewhere [18]. The important results will be summarized below.

$$\tilde{T}(\omega) = \frac{\tilde{E}_{sample}(\omega)}{\tilde{E}_{ref}(\omega)} \tag{2.7}$$

For a slab of thickness L with permittivity ε_2 and permeability μ_2 (we're in CGS unit), the transmission function of a plane wave going from medium 1 (such as air) through the sample and exit back to medium 1 at normal incident is:

$$\tilde{T}(\omega) = \tilde{t}_{1,2}\tilde{t}_{2,1} \exp^{i\frac{\omega}{c}L(\sqrt{\tilde{\varepsilon}_2\tilde{\mu}_2}-\sqrt{\tilde{\varepsilon}_1\tilde{\mu}_1})} \tag{2.8}$$

$$\tilde{t}_{1,2} = \frac{2}{\sqrt{\frac{\tilde{\mu}_1\tilde{\varepsilon}_2}{\tilde{\mu}_2\tilde{\varepsilon}_1}} + 1} \tag{2.9}$$

17

At normal incident, equation 2.9 is the amplitude transmission at the interface of two general medium (no assumption about μ) [12]. The complex $\tilde{T}(\omega)$ is an experimentally determined quantity. We can assume that $\varepsilon_1 \approx 1$ and $\mu_1 \approx 1$ because the sample is typically kept in a pure He gas environment. That leaves $\tilde{\varepsilon}_2$ and $\tilde{\mu}_2$, the quantities of interest, as the unknown to be extracted from our experiment. This leads us to acknowledge the limitations of this measurement. If the material is non-magnetic, e.g. $\tilde{\mu}_2 = 1$, then the equation 2.8 can be numerically solved with minimal effort. However, if $\tilde{\mu}_2 \neq 1$, we have to solve for 4 unknown quantities (2 unknown complex quantities) from the 2 experimentally determined quantities. This situation can be resolved by simultaneously measuring the reflectivity of the sample. Such experiment have been demonstrated [20, 21]. Another scheme to get around this situation with only the transmission measurement will be discussed in chapter 4.

TDTS is a polarization sensitive measurement. The optical properties of anisotropic materials require this sensitivity. In an anisotropic material, it is necessary to express the transmission function as a tensor. At normal incident with a sample, represented by the transmission tensor $\tilde{\mathbf{T}}$, an experiment can be "simulated" by the following equation:

$$\mathbf{E_f} = \mathbf{T} \cdot \mathbf{E_i} = \begin{bmatrix} T_{xx} & T_{xy} \\ T_{yx} & T_{yy} \end{bmatrix} \cdot \begin{bmatrix} E_x \\ E_y \end{bmatrix} \tag{2.10}$$

Wire-grid polarizers (QMC Instruments) can be placed in the beam path to change the incident and transmitted polarization. We use a pair of polarizers to select which component of the $\mathbf{T}$ matrix to probe in our measurement. The polarization can also be used to selectively excite resonances, such as magnon, phonon, or electronic levels.

2.2.2 Raman Spectroscopy

Initially discovered by scattering monochromatic incoherent light off of various molecules and liquids, Raman spectroscopy has become a standard tool when it comes to probing molecular and crystal vibrations [22, 23]. Raman scattering is an inelastic scattering effect. Monochromatic light is scattered off of a sample. The scattered light can have frequencies

different from the incident light's frequency. The effect can be described as the exchange of energy from the incident EM radiation to the molecule or crystal. By measuring the scattered light and determine the change in frequencies, we can determine the characteristic energy of the phenomenon in our sample. In solids, these phenomena range from phonon, magnon, to crystal field energy levels, etc.

In principle, there are two processes that simultaneously happen as the incident light interacts with the sample 2.6. First the Stokes process where the light loses energy, while the second is the anti-Stokes process where the light gains energy. Typically, this energy shift can come from a phonon, which is a quantum of energy that is associated with the collective lattice vibration in a crystal. The processes can be thought of as the creation (Stokes) or destruction (anti-Stokes) of a phonon by the incident light. Our ability to observe of these effects largely depends on the Raman selection rules. The selection rules for Raman and infrared (IR)/THz spectroscopy will be described in a later section.
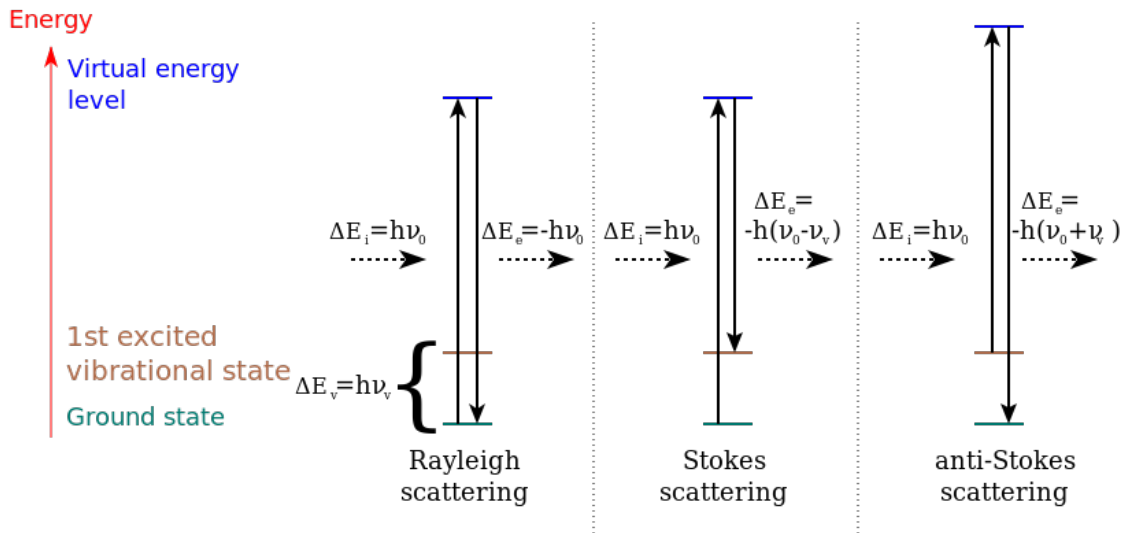
Figure 2.6: **Raman Scattering**. Schematics of the Raman scattering process. The lowest horizontal lines represent the ground state of a system. An incident light beam with photon energy $h\nu_0$ excite the system into an excited state. This excited state can decay into a different state. Image taken from Wikipedia [5].

The work that I've done was on a commercial Raman spectrometer, Renishaw inVia Raman Microscope. Coherent radiation coming from a laser is focused onto the surface of the sample by a confocal objective. The irradiated spot size is approximately $\sim 1~\mu m$. In the backscattering measurement geometry, the reflected light is collected and collimated by the same objective and sent to a spectrometer. Before coming to the spectrometer, a filter is in place to block off the original laser frequency. The system is capable of measuring frequency shift of $100cm^{-1}$ to $3200cm^{-1}$ (or $12.4meV$ to $396.7meV$). This system also includes a pair of polarizers to control the polarization of the incident light (before sample) and scattered light (after sample). These polarizers typically operate at either parallel or crossed configuration. The use of these polarizers will be made apparent in the discussion of the Raman selection rules.

2.3 Crystalline symmetry

In general, all 9 elements of the tensor in Eq. 2.6 are not unique inside a crystal. Multiple tensor elements might be equal to each other, or zero. There is a principle that reduces the number of independent components of any phenomenological tensor (of any rank) in a crystal. This is known as Neumann's principle (which, interestingly, was formulated by Pierre Curie in term of *asymmetry*). Neumann's Principle states that any property tensor of a crystal must remain invariant under any transformation that leaves the crystal unchanged[24, 25].

A symmetry operation (or element) of a crystal is any transformation that leaves it unchanged. An example of a symmetry operation can be seen in a some cubic crystal, such as NaCl. Rotating the unit cell by 90 degrees about the normal to any of its faces would leave it unchanged 2.7. Another symmetry operation of a cube is a 120 degrees rotation around any of the cube diagonal. Each crystal type has a set of symmetry operations that form a discrete symmetry group. The example here with the perfect cube has the point group symmetry O_h, which has 48 of these unique symmetry operations. In this section, I will give a quick introduction to these crystallographic symmetries, and show that

20
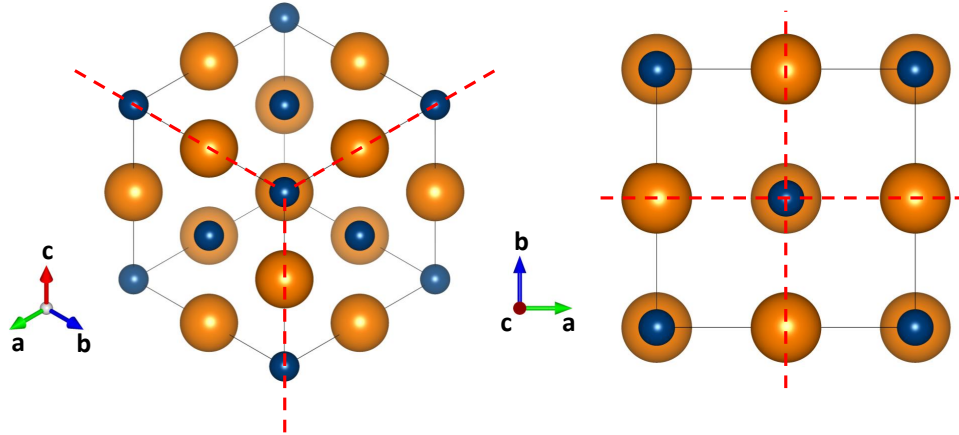
Figure 2.7: **Unit Cell of NaCl**. Some symmetries of salt crystal, NaCl. Na is represented by blue, Cl by red. Looking along the cubic body diagonal [111] axis (left) and [001] axis (right). The red-dash lines are equivalent under 120° rotation (C_3) on the left and 90° (C_4) on the right.

understanding these concepts is crucial to understanding the spectroscopic data.

There are 230 crystallographic space groups (3-D) [10]. If magnetism is taken into account, there are 1651 magnetic space groups. The *space groups* are generated from the 32 crystallographic *point groups*. It's adequate to limit this introduction to the point groups. The symmetry elements within each group must obey the usual requirements of group theory: closure, identity element, associativity, and inverse element. The point groups have combinations of the following symmetry operations: 1-fold rotation (identity), 2-fold rotation, 3-fold rotation, 4-fold rotation, 6-fold rotation, inversion, and mirror symmetry. Each symmetry element are defined to be oriented along some direction within the crystallographic unit cell.

The symmetry operations in each space or point group have been tabulated elsewhere.

$\mathbf{D_{2d}}$	E	$2S_4$	$C_2(z)$	C_2'	$2\sigma_d$	Linear, Rotation	Quadratic
A_1	+1	+1	+1	+1	+1	-	$x^2 + y^2, z^2$
A_2	+1	+1	+1	-1	-1	R_z	-
B_1	+1	-1	+1	+1	-1	-	$x^2 - y^2$
B_2	+1	-1	+1	-1	+1	z	xy
E	+2	0	-2	0	0	$(x,y)(R_x, R_y)$	(xz, yz)

Table 2.1: **Character table for tetragonal point group D_{2d} (or $\bar{4}2m$)**

One can simply look up the character table from any crystallographic online or printed resource. In condensed matter physics, there are various books that deal group theory and discrete symmetry [24–28]. The following discussion is by no mean comprehensive. A quick summary of how to use the tabulated information in spectroscopic measurements is followed. For example, this is a character table of the point group D_{2d} (or $\bar{4}2m$):

On the top row, $E, 2S_4, C_2, 2C_2', 2\sigma_d$ are the symmetry elements (classes) of this point group. E is the identity operation. S_4 is an improper rotation (roto-inversion), where there a 4-fold rotation (90 degrees rotation) followed by an inversion operation, $(x, y, z) \rightarrow (-x, -y, -z)$. The axis of rotation of S_4 is considered the principal axis, z. C_2 is a 2-fold rotation (180 degrees rotation) sharing the axis with the S_4. C_2' is another 2-fold rotation, around a different axis. σ_d is the mirror plane, containing the rotation axis of S_4.

The left-most column contains the irreducible representations of the group. In this context, a representation of one of the point groups can be defined as a set of matrices, each corresponds to a single symmetry element of the group. The irreducible representations cannot be made block diagonalized by any similarity transformation. The letters have the following meaning: A and B are 1-dimensional representations; E is 2-dimensional; and T is 3-dimensional. The dimensionality mentioned here represents the size of the matrix. The number subscripts (of any representation) follow certain rules, which would require more mathematical background to explain. In point groups with inversion symmetry, the subscripts u and g, short for *ungerade* and *gerade*, meaning odd and even under inversion

respectively. Its importance will be clearer when we discuss the phonon selection rules.

The numbers with + and - are the characters of each symmetry element in a particular matrix representation. The character of a matrix is the sum of the diagonal elements of the matrix. The characters of each element are unique within each irreducible representation (the matrix representations are not however). Each *irreducible representation* in the group can be expressed with different orthogonal basis functions. These functions can be linear, rotational, quadratic, etc. As a convention, the functions in these character tables are proportional to the real electronic wave function of the Hydrogen atom (in space). A shorthand way to understand these basis functions is: something that has the symmetry of say B_2 would transform like the functions z or xy under the symmetry operations of the group D_{2d}. In most character tables, linear, rotational, and quadratic basis functions are listed.

There are 8 symmetry elements in the D_{2d} point group. One might notice that by combining certain the elements, we can obtain the other elements of the group. This is in fact the closure property of a group. Careful examination of all the possible combinations will reveal that we only need 2 of these elements to generate the rest. These are called the generators of the group. They are tabulated in various texts, like the one by Birss[24]. For D_{2d} these generators are S_4 and C_2'. The matrix representation (in 3D) of S_4 around the high symmetry axis z and C_2' around a perpendicular axis y:

$$\Gamma(C_2') = \begin{bmatrix} -1 & 0 & 0 \\ 0 & 1 & 0 \\ 0 & 0 & -1 \end{bmatrix} \tag{2.11}$$

$$\Gamma(S_4) = \begin{bmatrix} 0 & -1 & 0 \\ 1 & 0 & 0 \\ 0 & 0 & -1 \end{bmatrix} \tag{2.12}$$

2.3.1 Example of application of Neumann's Principle

To demonstrate Neumann's Principle, we will examine $\tilde{\varepsilon}$ in the point group D_{2d}. One only need to consider the generators of the group in order to reduce the number of independent tensor components. Let's first define how a property tensor of rank n is transformed by a symmetry operation (rank 2 tensor):

$$T_{ijk...n} = S_{ip}S_{jq}S_{kr}...S_{nu}T_{pqr...u} \tag{2.13}$$

Here, a property tensor T is transformed by a symmetry operation S. Each index represent a Cartesian coordinate. Each of the indices $p, q, r, ...u$ are summed over the set of $x, y, and z$. For $n = 2$, this equation is equivalent to the usual matrix transformation $T = S^{-1}TS$.

$$T_{ij} = S_{ip}S_{jq}T_{pq} = S_{ix}(S_{jx}T_{xx} + S_{jy}T_{xy} + S_{jz}T_{xz}) + ... \tag{2.14}$$

By applying the matrices in eq. 2.11 and 2.12 in place of S, and $\tilde{\varepsilon}$ in eq. 2.6 we get the following matrices:

$$\tilde{\varepsilon} = \begin{bmatrix} \tilde{\varepsilon}_{xx} & -\tilde{\varepsilon}_{xy} & \tilde{\varepsilon}_{xz} \\ -\tilde{\varepsilon}_{yx} & \tilde{\varepsilon}_{yy} & -\tilde{\varepsilon}_{yz} \\ \tilde{\varepsilon}_{zx} & -\tilde{\varepsilon}_{zy} & \tilde{\varepsilon}_{zz} \end{bmatrix} \tag{2.15}$$

$$\tilde{\varepsilon} = \begin{bmatrix} \tilde{\varepsilon}_{yy} & -\tilde{\varepsilon}_{yx} & -\tilde{\varepsilon}_{yz} \\ -\tilde{\varepsilon}_{xy} & \tilde{\varepsilon}_{xx} & \tilde{\varepsilon}_{xz} \\ -\tilde{\varepsilon}_{zy} & \tilde{\varepsilon}_{zx} & \tilde{\varepsilon}_{zz} \end{bmatrix} \tag{2.16}$$

Neumann's principle implies that the matrix in 2.15 has to be equal to 2.6. We can then see that $\tilde{\varepsilon}_{xy}, \tilde{\varepsilon}_{yx}, \tilde{\varepsilon}_{yz}, \tilde{\varepsilon}_{zy} = 0$. Setting 2.16 equal to 2.6, $\tilde{\varepsilon}_{xz}, \tilde{\varepsilon}_{zx}$ also vanish while $\tilde{\varepsilon}_{xx} = \tilde{\varepsilon}_{yy}$.

As a result, the dielectric tensor has only two unique elements:

$$\tilde{\varepsilon} = \begin{bmatrix} \tilde{\varepsilon}_{xx} & 0 & 0 \\ 0 & \tilde{\varepsilon}_{xx} & 0 \\ 0 & 0 & \tilde{\varepsilon}_{zz} \end{bmatrix} \tag{2.17}$$

In addition to having the symmetries imposed by S_4 and C_2' (eq. 2.11,2.12), there is an intrinsic symmetry to these rank 2 tensors that we must acknowledge. Following the discussion from Landau Lifshitz[29, 30], we note that $\tilde{\varepsilon}$ is a symmetric tensor (or $\tilde{\varepsilon}_{ij} = \tilde{\varepsilon}_{ji}$. The classical explanation for this property is briefly mentioned in the both texts using thermodynamic potential and the fluctuation dissipation theorem. With transport tensors, such as with the electrical conductivity and thermal conductivity σ and κ, Onsager's reciprocal relations state not only that these tensors are symmetric, but also relate the Peltier and Seebeck tensors [25, 31, 32].

The situation becomes slightly more complicated when time reversal symmetry is broken by either spontaneous magnetization or an applied magnetic field. The text by Cracknell [25] details a general method of applying Neumann's principle with the time reversal symmetry operation.

$$\sigma_{ij}(\mathbf{H}) = \sigma_{ji}(-\mathbf{H}) \tag{2.18}$$

$$\sigma_{ij}(\mathbf{H}) = \sum_p \sum_q S_{ip} S_{jq} \sigma_{pq}^*(\mathbf{H}) \tag{2.19}$$

Equations 2.18 represent the intrinsic symmetry mentioned above, in the present of a magnetic field $\mathbf{H}$. $\mathbf{H}$ can come from any internal or external field, or some combination. Eq. 2.19 is the modified version of Eq. 2.13. It is to be used when applying Neumann's Principle on a magnetic system's symmetry (the composite of time reversal and a spatial symmetry operation would leave the spin system unchanged). One should note that Eq. 2.19 works at finite frequency and any general magnetic field $\mathbf{H}$ [25].

What has been demonstrated above can be served as an example for analyzing different optical property tensors in an anisotropic crystal. Within the linear regime, THz

25

spectroscopy only probe two components of a 2x2 matrix in a single measurement (Jones Matrix formalism). Within the same crystal class (D_{2d} *is tetragonal*), the dielectric tensor looks the same for multiple members of that class (eq. 2.17 is true for point groups D_4, C_{4v}, D_{2d}, and D_{4h}). However, the analysis above becomes extremely useful in non-linear measurements [33]. The second order susceptibility can be described by a rank 3 tensor. Changes of the point group symmetry would result in a drastic change of the tensor. These tensors have been worked out to higher orders and tabulated online and in various texts (like the one by Birss [24]).

2.4 Basic selection rule

In most quantum mechanics textbooks, the selection rule for the transition between two states due to an oscillating electric field is derived (for example, Shankar[34]). These derivations boil down to calculating the probability of transition from an initial to a final state via Fermi's golden rule. Besides from the energy conservation requirement, the probability of transition depends on the matrix element $\langle f | \mathcal{H}' | i \rangle$.

$$P \propto | \langle f | | \hat{\mathcal{H}}' | i \rangle |^2 \tag{2.20}$$

$$\mathcal{H}'_{em} = -\frac{e}{mc} \mathbf{p} \cdot \mathbf{A} \tag{2.21}$$

The electromagnetic interaction that give rise to the electric dipole transition is shown in equation 2.21 [26]. Here, $\mathbf{p}$ is the electron's momentum and $\mathbf{A}$ is the vector potential. $\mathbf{p}$ is odd under inversion while $\mathbf{A}$ is not. It can be sen immediately that the matrix element $\langle f | \mathcal{H}'_{em} | i \rangle$ is only non-zero if the initial and the final state have different parity (odd or even under inversion). This is the basic result for the electric dipole selection rule.

It turns out that D_{2d} is not such a good point group to give an example for this selection rule. Since the group lack inversion symmetry, the wave functions representing the ground state have no definite parity (they are neither odd nor even). The probability integral doesn't necessarily vanish base on the above argument. It will be shown in $Sr_2FeSi_2O_7$ (a

crystal that has D_{2d} point group symmetry) that not only the phonons are excitable by both Raman and infrared spectroscopy, but transitions between the d-electrons electronic states are possible. The following discussion is for crystals that are inversion symmetric.

2.4.1 Phonons

In a solid of N molecules, there are 3N degrees of freedom. There would be 3N normal modes, or phonons (3 of which are acoustic modes with $\omega(\mathbf{k} = 0) \equiv 0$. The derivation of the selection rules for these phonons would be complicated story. Fortunately, group theory provides the necessary framework to quickly determine which phonons are excitable by THz or Raman spectroscopy [26]. To understand why this method should work, one should think about the Hamiltonian or equation of motion describing the lattice vibrations and how it must remain invariant under the symmetry operations belong to the crystal's symmetry group. As a consequence, the (block) diagonalized and hence the eigen modes of the Hamiltonian or the dynamical matrix can be classified by the symmetry group's irreducible representation.

In optics, the phonon/magnon excitations are typically at the Brillouin Zone Center or $\mathbf{k} \approx 0$. The ground state would be the unperturbed lattice (has the symmetry of the totally symmetric representation A_1). The final state would be one of the lattice vibration normal mode. The symmetry group at $\mathbf{k} \approx 0$ is the same as the crystallographic symmetry ($\mathbf{k} \approx 0$ is equivalent to long wavelength oscillation, or the whole lattice moving in unison).

Since group theory has readily characterized the symmetry of these normal modes, it is a matter of applying equation 2.20 to find out the selection rules for these modes. The THz and infrared Hamiltonian transforms like a vector (as mentioned above). This means that in order for the probability of transition (equation 2.20) to be non-zero, the phonon final state must have the symmetry of a *linear* basis function. Ultimately, the calculation that must be done is an integral over all spatial coordinates. If the integrand has odd parity, the integral vanishes. Additionally, the electric field vector (momentum of the electron) must not be perpendicular to the symmetry function of the phonon.

This bring us to the Raman selection rule. It is similar to the infrared and THz spec-

troscopy. However, as explained in 2.2.2, the Raman process involves two different electric fields, E_i and E_s incident and scattered. The Raman interaction Hamiltonian looks like this:

$$\mathcal{H}'_{Raman} = -\frac{\Delta\overleftrightarrow{\alpha}}{2}\mathbf{E_i}\mathbf{E_s}cos(\omega \pm \omega_0) \tag{2.22}$$

Here, ω_0 is the phonon frequency, $\overleftrightarrow{\alpha}$ is the polarizability tensor ($\mathbf{p} = \overleftrightarrow{\alpha} \cdot \mathbf{E_i}$). The transformational properties of $\mathcal{H}'_{Raman}$ is that of $\overleftrightarrow{\alpha}$ [26]. $\overleftrightarrow{\alpha}$ is a second rank symmetric tensor and has the same transformational properties as the quadratic basis functions. A similar argument to the THz and infrared selection rule can be made. The probability integral vanishes if the integrand has odd parity. This means that *the Raman transition can only occur between states of the same parity*. Since the ground state is totally symmetric, a phonon has to transform like the *quadratic* basis functions in order for it to be Raman active.

2.4.2 Magnons

The classical treatment of ferromagnetic or antiferromagnetic resonances can give us a useful insight as to how these magnetic resonances can be excited [35]. For a small perturbation coming from an oscillating magnetic field, its direction needs to have a component transverse to the magnetic moment in order to excite the antiferromagnetic resonance. This can be understood classically as the application of a torque on the moment by a magnetic field, $\tau = \mathbf{H}_\omega \times \mu$. The torque τ is only non-zero if the applied oscillating field $\mathbf{H}_\omega$ is transverse to the magnetic moment μ.

A quantum mechanical treatment can also be done. The approach for ferromagnetic magnons can be found in Ashcroft and Mermin [10]. To summarize, a magnon can be thought of as changing the spin state by 1, $|S\rangle \to |S \pm 1\rangle$. Since we are dealing with an ordered system, the creation of a magnon can mean the flipping of the spin on a single atom, or the superposition of many. This flipping of spin can be achieved by a raising or lowering operator. These operators only have non-diagonal elements in the lab frame. What this

means is that only the transverse magnetic field (transverse to the ordered moment) can create a magnon.

2.4.3 General application of group theory on selection rules

Here is the general rules from [26]. The arguments come down to finding when the matrix element in eq. 2.20 is non-zero. Once the transformation properties of the initial, final state and the Hamiltonian are found, the *direct product* between the initial state representation , Γ_i, and the perturbation Hamiltonian representation, $\Gamma_{\mathcal{H}'}$ should be calculated. The direct product in all space and point groups are tabulated. The result of this direct product must contain the representation of the final state in order for the matrix element $\langle f | |\hat{\mathcal{H}}' |i\rangle$ to be non-zero.

Chapter 3
MULTIFERROICITY IN SR$_2$FESI$_2$O$_7$

3.1 Introduction

Multiferroics belong to the class of materials that host more than one type of ferroic order, i.e. (anti)ferroelectricity, (anti)ferromagnetism, ferroelasticity, etc. In each of these phases of matter, multiple order parameters exist simultaneously. There are two types of multiferroics, type I ("conventional") and type II ("unconventional"). One can imagine a situation that a coincident can occur inside some material where it orders antiferromagnetically and then ferroelectrically at a different temperature. This is type I. The much more interesting type II multiferroic has the onset of both order parameters happening simultaneously. This implies that the order parameters are coupled. When this coupling occurs, for example between the magnetization $\mathbf{M}$ and electric polarization $\mathbf{P}$, exotic properties can emerge. It has been demonstrated that $\mathbf{P}$ can be controlled by an external magnetic field, and $\mathbf{M}$ can be controlled by an external electric field in TbMnO$_3$ and TbMn$_2$O$_5$ [36–38].

The prospect of electrically controlling the magnetization and vice versa is an enticing one. Capacitive switching of magnetic memory promises significantly reduce the energy loss of generating a magnetic field via the current heating effect. Unfortunately, the temperatures where these coupling would occur tend to be only a few Kelvins above absolute zero. Significant efforts have been made in artificially creating multiferroics out of heterostructures of ferroelectrics and (anti)ferromagnetic materials[39, 40]. The hope is to use material engineering to create a feasible room temperature or near room temperature device with these heterostructures.

Time-Domain THz spectroscopy has proven to be a key technique to study many multiferroics. Due to the coupling between $\mathbf{P}$ and $\mathbf{M}$, some of the phonons and magnons can also become coupled. This leads to a hybridization between these two cooperative phenomena (dubbed the electromagnon). Exotic optical properties such as directional dichroism and magneto-chiral dichroism have been observed in the multiferroic $Ba_2CoGe_2O_7$ (BCGO)[41, 42] in the THz frequencies. In BCGO, $\mathbf{M}$ and $\mathbf{P}$ are coupled below the ordering transition temperature $T_{Neel} \sim 6$ K. The coupling results in an absorption mode that is both electrically and magnetically active [42–44]. An interesting feature of these phenomena is that the electrically-active magnon (or electromagnon) mode survives above the Neel temperature, which has so far not received a full explanation. The electromagnon is a signature of the multiferroic phase, and is one of the most exciting discoveries in the area of quantum magnetism in the last ten years.

It was recognized early in the multiferroic renaissance that the Dzyalonshinskii-Moriya (DM) interaction is crucial for the coupling between ferroelectricity and spiral magnetic order [45–47]. The origin of the DM interaction is the spin-orbit coupling (SOC) [48–50], and thus SOC is at the center of the phenomena of magnetically induced ferroelectricity. Although SOC can also generate dynamical effects [51], the dynamical response of electromagnons in the multiferoic families of $RMnO_3$ and RMn_2O_5 (where R is a rare-earth ion) has been explained by the symmetric Heisenberg exchange-striction [43, 52] without the need for SOC. One of the exceptions is in fact BCGO, where SOC has to be explicitly taken into account to explain the electromagnons in that system [53–58]. Surprisingly, however, these theories have not included the effect of tetragonal distortion of the CoO_4 tetrahedra in the explanation of the static and dynamical properties of BCGO. This omission is even more glaring as highlighted by the fact that the tetragonal distortion of the tetrahedra is of 13% compression with respect to a perfect tetrahedron. For comparison, we find that the compression in SFSO is $\sim 17\%$. Just recently the effect of this distortion on the electronic properties of BCGO and similar materials has been studied using first-principles calculations [59, 60]. We point out the fact that in BCGO, the magnetic ion is Co^{2+}, with a d^7 configuration in the 3d-orbitals; this contrast with SFSO where Fe^{2+} has a configuration of

d^6. Therefore, the many-body ground states to be considered for the low energy excitations in BCGO [55] and SFSO are fundamentally different. Thus, this distinction between the two compounds may explain the dissimilarities in their THz excitations.

In this chapter, we report the THz study above 7.5 K of $Sr_2FeSi_2O_7$ (SFSO), a material isostructural to BCGO (space group #113, $P\bar{4}2_1m$, Fig. 3.2). The single crystal SFSO samples show multiple absorption modes above the magnetic order transition temperature, $T_{Neel} \sim 5$ K [61]. These absorption modes can be understood as transitions between the spin-orbit and crystal field split ground state levels of the Fe^{2+} ion on a compressed tetrahedral environment. We find it crucial to consider this tetragonal distortion in order to explain the details of these magnetic excitations. We will discuss the shortcomings of this model and point to potential avenues for a better understanding.

3.2 Experimental Methods

The multiferroicity of $Sr_2FeSi_2O_7$ is briefly summarized here as the details will be reported elsewhere[61]. First of all, $Sr_2FeSi_2O_7$ undergoes a transition to an antiferromagnetic state at $T_N \sim 5$ K. Accompanying the magnetic transition, a small electric polarization along the c direction P_c appears below T_N; the value of P_c is approximately 3 $\mu C/m^2$ at T = 2 K. It is also found that both the magnitude of P_c and the transition temperature T_N change considerably under an external magnetic field along the [110] diagonal direction (H_{ab}); for instance, P_c at 2 K reaches ~ 50 $\mu C/m^2$ for H_{ab} = 2.5 T and T_N becomes 2.5 K at H_{ab} = 6.5 T. It would be noteworthy that the evolution of P_c with H_{ab} below T_N is adequately accounted for in terms of the spin dependent p-d hybridization model proposed for $Ba_2CoGe_2O_7$[55].

We used a home-built time-domain terahertz spectrometer (TDTS) with photoconductive antennas as source and detector of THz radiation. This technique has recently risen to the forefront of the study of novel excitations in quantum magnets [3, 62, 63]. It has the advantage of being of high energy resolution for Brillouin zone-center excitations, and it does not need as large single crystals as other techniques. TDTS also has the advantage

of a phase sensitive measurement, which means that one can obtain the complex optical constants of the material. The samples were mounted inside a closed-cycle cryostat with optical access windows that is capable of cooling to 7 K. By comparing the frequency components of a THz pulse that has passed through the sample to one reference without a sample, we can extract the transmission coefficient, $t(\omega)$, as a function of frequency. The absorption coefficient can then be extracted from the transmission data as -$\log t(\omega)/d$, where d is the thickness of the crystal. In this experiment, we fitted each absorption peak with a Lorentzian lineshape, characterized by the absorption peak frequency, its full width at half maximum, and by its spectral weight.

We studied two single crystals of SFSO: one is a-plane cut $\sim$1150 μm thick; and the second one, $\sim$460 μm thick, is c-plane oriented. In order to clarify the nature of the absorption modes with their selection rules, we used a wire grid polarizer to linearly polarize the THz pulse along the different crystalline axes. To avoid birefringence in the a-plane sample, we measured the sample with the THz electric field, e$_\omega$ polarized parallel to the b axis, and with e$_\omega$ ∥c. As expected, the c-plane sample did not show any birefringence due to its tetragonal crystal structure. The single crystals were grown using a floating zone method in a reducing atmosphere with feed rods prepared through a solid-state reaction.

Single crystal X-ray diffraction was performed at Ohio State to the space group and crystalline axes. At room temperature, the unit cell parameters are $a = 8.1121$ and $c = 5.1204$ Angstrom. The point group of this crystal was discussed in chapter 2, as D_{2d}. Although the space group is fairly complicated (there's a screw axis), and there are many different atoms in the unit cell, D_{2d} is also the point group of the Fe sites. The consequences of having a distorted tetrahedron around each Fe site will be discuss later on.

3.3 Results

We measured the absorption spectra of $Sr_2FeSi_2O_7$ from 7.5 to 300 K, and we identify three measurable absorption modes with frequencies of $\sim$ 0.6, 1.0, and 1.4 THz, as shown in Figure:3.1(D), labeled as α, β, and γ, respectively. At 7.5K, the α mode is the strongest

among these with absorption coefficient around a few tens of cm^{-1}, comparable to BCGO's electromagnon mode [42]. Meanwhile, the β mode is virtually absent at 7.5 K but gradually increases in strength and peaks at 20 K. The γ mode at 1.4 THz is the weakest of the three. It is clear from the behavior of the spectral weight of the β mode (see figures 3.1(D)-(F), and figure 5.3(A)) that it corresponds to a transition between two excited states, as its strength first increases and then decreases with temperature, a clear indication of population of the excited states with temperature. The α and γ absorptions, on the other hand, are clearly from a ground state to two different excited states. This phenomenology can be captured in a simple three-level system depicted in the inset of figure 3.1(D) and in figure 3.4. The details will be discussed below.

Around 100 K, another absorption mode starts to move down into our frequency range, completely dominating the spectra at room temperature. We believe this high frequency-high temperature mode is consistent with a polar phonon. Interestingly, the peak positions of the α and β modes are red shifted with increasing temperature, cf. fig. 5.3, a behavior typical of an order parameter-type phase transition. However, there is no known phase transition above $\sim$ 5 K in this material. Therefore, our simple phenomenological three-level system will need to be expanded in order to explain these frequency shifts.

All three modes exists in all orientations of the THz electric field e_ω with respect to the crystal axes, see figures 3.1(D)-(F). This suggests that these modes are active under both the electric and magnetic dipole selection rule. This is similar to the behavior of the low energy excitations found in BCGO [42]. We find this behavior in the paramagnetic state of SFSO as opposed to the magnetically ordered one in BCGO. It is also the case, however, that the 1 THz electromagnon in BCGO survives to temperatures higher than the Néel temperature, and has been suggested to be a *spin-stretching* mode [56]. In SFSO, the main features of the polarization selection rules of the three modes are: 1) when the magnetic field of the THz is in the $a-b$ plane, $\text{h}_\omega \parallel b$, the α mode has the same intensity regardless of the direction of the THz electric field e_ω, 2) this also applies to the γ mode. 3) When $\text{h}_\omega \parallel c$ or $\text{e}_\omega \parallel a-b$ plane, all three modes are much weaker than in the other two orientations. This behavior suggests that the modes are mainly of magnetic dipole character in the $a-b$ plane,

Table 3.1: **Selection rules for the excitation of the observed absorption modes**. The absorption modes exist in all 3 configurations, as represented in this table of maximum spectral weights. The values are normalized to the largest absorption spectral weight of 0.37 mm^{-1}Hz. The values for α and γ are from 7.5K, while the β values are from 20K. Here e_ω and h_ω are the electric and magnetic fields of the THz pulse, respectively. a, b and c are the crystallographic axes.

	$h_\omega \parallel$ b & $e_\omega \parallel$ c	$h_\omega \parallel$ b & $e_\omega \parallel$ a	$h_\omega \parallel$ c & $e_\omega \parallel$ b
α	77%	100%	38%
β	43%	70%	19%
γ	23%	32%	28%

$h_\omega \parallel b$, and are only weakly electric dipole on the same plane, $e_\omega \parallel b$. This is summarized in table 3.1.

3.4 Discussion

We can begin understanding the nature of these excitations by utilizing a single site picture of the Fe^{2+} ion in the crystal field environment of a compressed tetrahedron. Low et al. [6] showed how the energy levels of the Fe^{2+} ion are split due to cubic crystal fields, including tetrahedral symmetries. These predictions were somewhat confirmed by Slack et al. [64] in the THz range where Fe^{2+} occupies a tetrahedral site in a ZnS matrix. In this case, however, Fe^{2+} ions are very diluted and do not interact with each other. Recent interest has been given to the excitations of a regular lattice of tetrahedrally coordinated Fe^{2+} in the material FeSc$_2$S$_4$ [3, 65]. It is thought that this material does not magnetically order, however next-nearest neighbor exchange has been used to theoretically explain the experimental results [66]. The effect of this exchange interaction between Fe^{2+} sites is to strongly renormalize the energies of the 5-fold split ground state term, and it also gives a dispersion in momentum space to the otherwise dispersionless single-site excitation.

Fe^{2+} has a 3d^6 (L=2, S=2) electronic configuration in free space (^{5}D term), but in Sr$_2$FeSi$_2$O$_7$ it occupies the 2a Wyckoff position in the P$\bar{4}2_1$m space group that has S$_4$ ($\bar{4}$) site symmetry. This site symmetry corresponds to 4 O^{2-} ions located at the vertices of

a tetrahedron compressed along the [001] crystallographic direction. We performed single crystal X-ray diffraction on our samples and obtained a compression of approximately 17%. We therefore model the electronic structure, following Low et al. [6]'s Table I in Appendix I, assuming an energy hierarchy of $\Delta \gg \delta \gg \lambda$, where Δ is the E–T_2 tetrahedral crystal field splitting, δ is the tetragonal compression splitting A–B, and λ is the spin-orbit interaction energy. In this limit, in the high-spin configuration and following Hund's rules, the ground state is a spin-orbital singlet $|E_0\rangle$ (eqn. 3.1), and the first two excited states are doublets up to second order in λ, $|E_1\rangle$ (eqn. 3.2) and $|E_2\rangle$ (eqn. 4.3). Their wave functions to first order in λ are (the basis for this expansion are the states $|L_z, S_z\rangle$, where both L_z and S_z go from -2 to +2):

$$|E_0\rangle = |0,0\rangle + x\left(\sqrt{6}\,|+1,-1\rangle + \sqrt{6}\,|-1,+1\rangle\right) + \mathcal{O}(\lambda^2) \tag{3.1}$$

$$|E_1^{\pm}\rangle = |0,\pm1\rangle + x\left(\sqrt{6}\,|\pm1,0\rangle + 2\,|\mp1,\pm2\rangle\right) + \mathcal{O}(\lambda^2) \tag{3.2}$$

$$|E_2^{\pm}\rangle = |0,\pm2\rangle + x\left(2\,|\pm1,\pm1\rangle\right) + \mathcal{O}(\lambda^2) \tag{3.3}$$

where $x = \frac{\sqrt{6}\lambda}{8(\Delta+\delta/4)}$, and $x \ll 1$. Note that the largest contribution to each of the states is derived from the $L_z = 0$ submanifold, and the S_z spin contribution changes by ±1 in each of the 2 excited states. This is derived from the fact that the lowest energy d-orbital, the z^2 orbital [67], is doubly occupied as given by the crystal field of the compressed tetrahedron [59, 60]. We note that for a perfect tetrahedron, the ground state manifold is split into five equally separated energy levels by the crystal field and SOC [6].

The second order spin-orbit Hamiltonian takes the form DS_z^2, which is the typical form for single ion anisotropy energy, where $D = \frac{\lambda^2}{16(\Delta+\delta/4)}$, we take as the zero of the energy the state $|E_0\rangle$. In this particular case, since $D \geq 0$, this is an easy-plane anisotropy. Figure 3.4 schematically shows the splitting of the ground state term by the crystal field and spin-orbit coupling, similar to Figure 4 in Low and Weger [6] which applies to the octahedral case. The states in figure 3.4 are now labeled by the irreducible representations of the point groups

belonging to each level of distortion, where SOC does not break any symmetry. We note that, whereas $|E_1^{\pm}\rangle$ is a doublet of E symmetry, $|E_2^{\pm}\rangle$ are two distinct states of B symmetry; they are accidentally degenerate only up to second order in λ. We can obtain a value for λ using $\Delta \approx 0.8$ eV [68] and $\delta \sim 0.1$ eV, and the predicted energy separation between $|E_0\rangle$ and $|E_2\rangle$, $\frac{12\lambda^2}{\Delta+\delta/4}$, and obtain an upper limit of $\lambda \approx 20$ meV. This value is lower than 100 meV, the free ion value of λ for Fe^{2+}[69].

Thus, the single-ion picture already contains a three-level structure that reproduces the basics of the experimental observations. Transitions between the states $|E_0\rangle$ and $|E_1\rangle$, and between $|E_1\rangle$ and $|E_2\rangle$ are magnetic dipole allowed as they are connected by an operator $S_{\pm} = S_x \pm iS_y$ that changes the S_z value by one. Therefore, a THz magnetic field polarized in the $a-b$ plane is able to make transitions between these states. The transition between $|E_0\rangle$ and $|E_2\rangle$, in this approximation, is only electric quadrupole since $\Delta S_z = \pm 2$ (terms of $\mathcal{O}(\lambda^3)$ and higher make the transition between $|E_0\rangle$ and $|E_2\rangle$ magnetic dipole as well). However, we note that because of the lack of inversion symmetry of the Fe^{2+} site, parity is not a good quantum number for the wave functions, admixtures of the ^5D ground term with higher energy terms of different parity (i.e. P and F terms) [6] are allowed. This mixing will make all the transitions between the three lowest states weakly electric dipole as well, as we find experimentally.

As we noted above, a feature of the data that cannot be explained by this single-ion picture is the fact that the lowest transition frequency has a very strong temperature dependence, whereas the second and third transition frequencies barely change, see figure 5.3(B). Therefore, the single-ion picture would need to be expanded to include the effects of interactions between the spin and orbital angular momenta of the Fe^{2+} ions at different sites. In addition, we highlight again that all of this phenomenology is occurring above the magnetically ordered transition temperature, and thus we expect that models such as those of Ish et al. [66] would be required to explain all of our experimental results. Below the ordering temperature, we expect to see antiferromagnetism of a similar type as BCGO. Magnetic ordering would lower the symmetry of the system even further, potentially causing splittings and further shifts in the absorption spectrum.

3.4.1 Magnetic field dependence

We investigate the behavior of these excitations in the paramagnetic phase and the antiferromagnetic phase in an applied static magnetic field, $\mathbf{H_0}$. One would expect the magnetic ordering to significantly change the spin orbital ground state. At zero magnetic field, we observed the same THz excitations below T_{Neel}, with a small blue shift in energy. Interestingly, the behavior with finite $\mathbf{H_0}$ is significantly different above and below T_{Neel}.

With the applied field out of the easy plane, above T_{Neel}, we observed a blue shift in the α excitation frequency, while the γ excitation remain unchanged (fig. 3.5). At this time, we still do not have a good theory for the change in the energy levels in magnetic field. The crystalline nature of the Fe^{2+} should be more complicated than the single ion picture. Interestingly, below the magnetic ordering temperature, both of the α and γ modes appear to split in field.

3.5 Summary

In summary, we have observed three spin-orbital transitions in the range between 0.2 THz and 1.7 THz in $Sr_2FeSi_2O_7$ using time-domain THz spectroscopy. These modes can be qualitatively explained by Fe^{2+} in a compressed tetrahedron crystal field environment where spin-orbit coupling splits the low energy manifold into a three-level structure with a singlet ground state and two doublet excited states. We estimate a spin-orbit coupling constant for Fe^{2+} of $\lambda \approx 20$ meV. We find it crucial to consider the effects of the compression of the tetrahedron, as without it, the low energy manifold would consist of five equally spaced energy levels [6]. The effect of this compression should be taken into account when explaining the THz excitations observed in BCGO as well. We also find that, although the single-ion picture can qualitatively explain many of our results, modifications will be needed to explain the strong shift with temperature of the transition frequency between the first two states. Measuring the THz absorption below T_{Neel} and under an applied magnetic field will shed more light onto the nature of the low energy excitations in $Sr_2FeSi_2O_7$, measurements which are now underway.
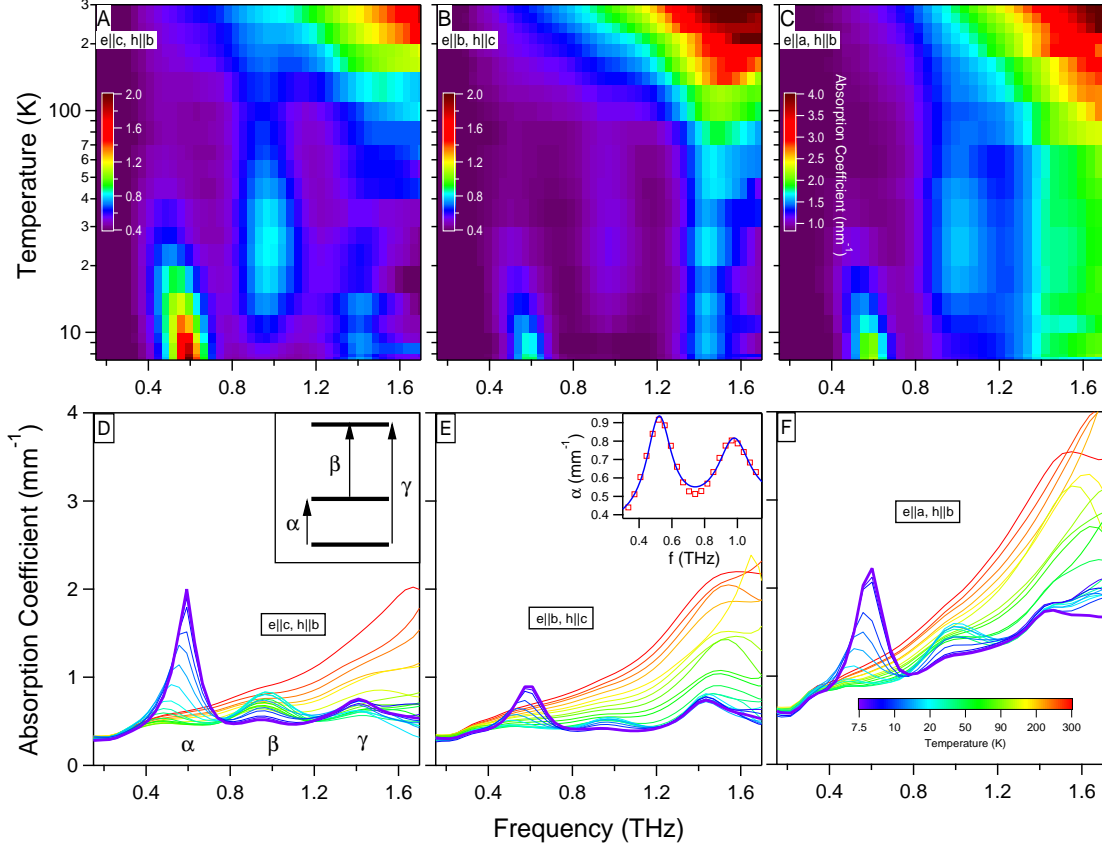
Figure 3.1: **Spin-Orbital THz absorption of $Sr_2FeSi_2O_7$**. False color maps of the absorption from 7.5 K to 300 K and below 1.7 THz for the (A) $e_\omega \parallel c$, $h_\omega \parallel b$, (B) $e_\omega \parallel b$, $h_\omega \parallel c$, and (C) $e_\omega \parallel a$, $h_\omega \parallel b$ configurations. The color corresponds to the absorption value as indicated in the scale bar in each individual panel. (D)-(F) Selected absorption traces for the same polarization configurations as in (A)-(C), respectively. The color scale bar in (D) applies to the three (D) through (F) panels. Please note that the temperature spacing between each line are not equally separated, but follow a semi-logarithmic increment from the lowest temperature. Inset in (D) shows the three level structure that is apparent in the temperature dependence of the absorption. Transitions are labeled as α, β, and γ as indicated. A different absorption mode appears at higher T, and dominates the other three. The inset in (E) shows an example of the raw spectrum (red square) at 15 K for $e_\omega \parallel c$, $h_\omega \parallel b$ along with its fitted line (solid blue).

39
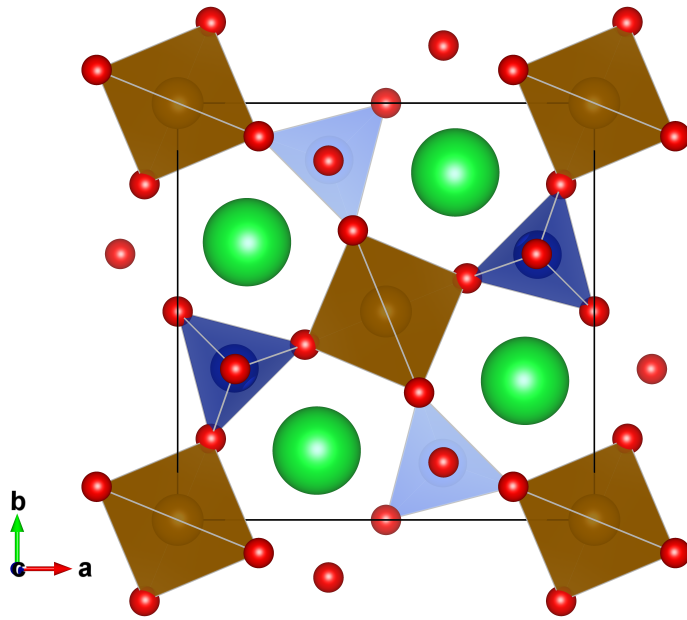
Figure 3.2: **Crystal structure of $Sr_2FeSi_2O_7$ (space group $P\bar{4}2_1m$), a-b plane**. The tetragonal unit cell can be seen by the dark box. The colors represent different atoms: Sr - green, Si - blue, Fe - brown, O - red. The atoms contributing to SFSO's magnetism is the Fe^{2+}. Fe is surrounded by a tetrahedral cage of oxygen. The crystal field environment give rise to the interesting effects measured in our study.
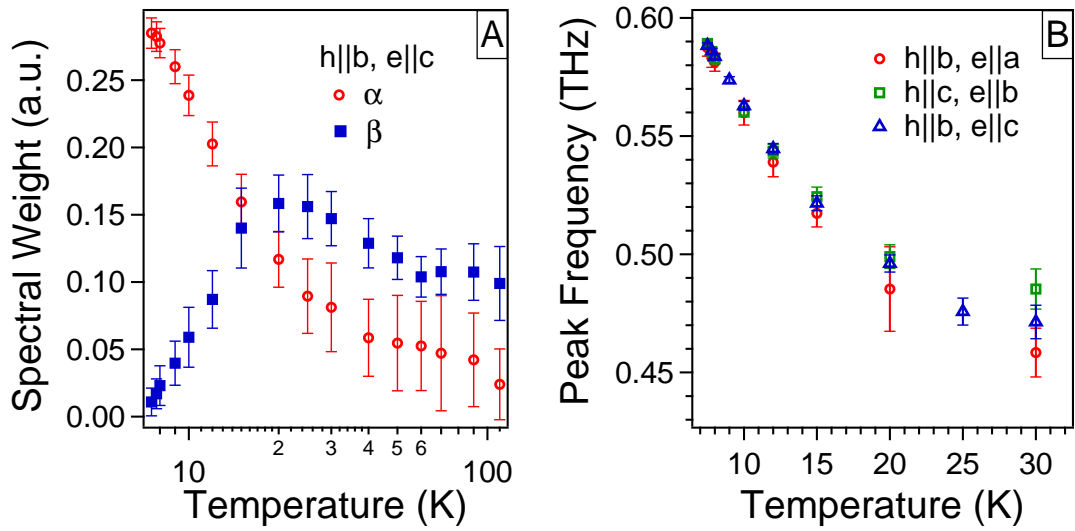
Figure 3.3: **Temperature dependence of transition parameters**. (A) Spectral weight of α and β transitions versus temperature in the polarization configuration $e_\omega \parallel$c, $h_\omega \parallel$b. The β transition clearly loses all its spectral weight towards zero temperature, a clear indication of a transition between two excited states. (B) Temperature dependence of the frequency of the α transition for the three polarization configurations explored in this work. Within error bars, the frequencies are identical, a signature of the same transition appearing in all polarization configurations.
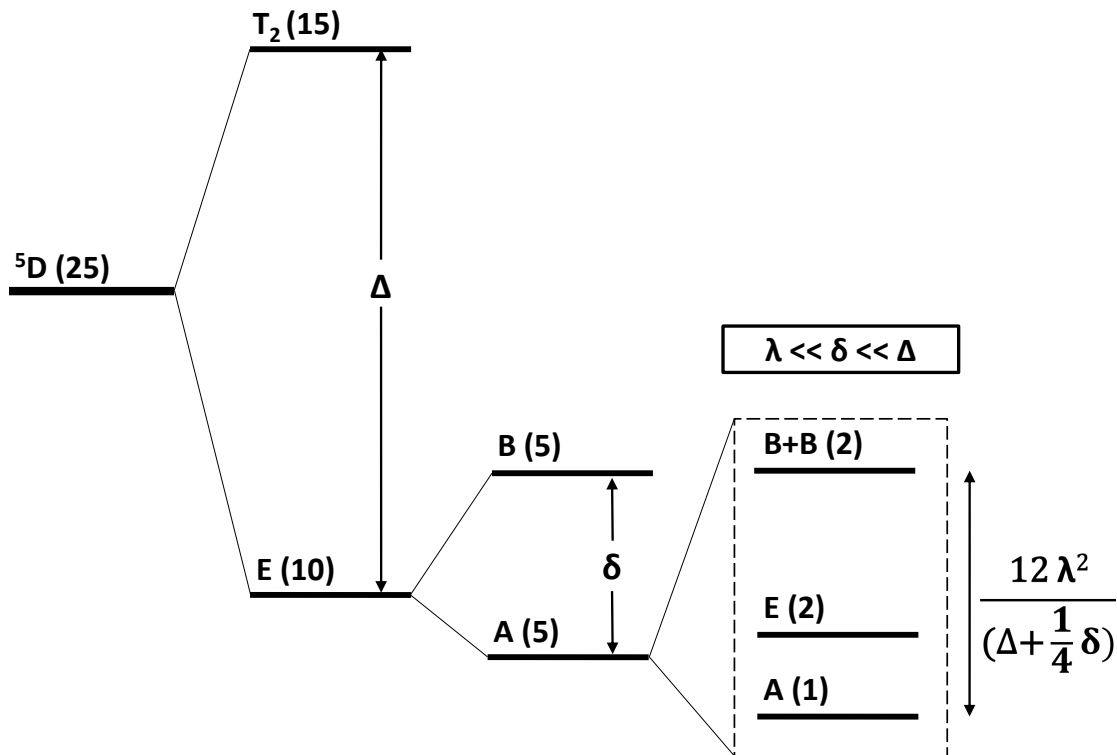
Free Ion Term	Tetrahedral Crystal Field (T_d)	Tetragonal Distortion (S_4)	2nd Order Spin-Orbit Coupling (S_4)

Figure 3.4: **Ground state splitting by crystal field and spin-orbit coupling**. Splitting of the Fe^{2+} term (^5D) in the S_4 crystal field environment and due to spin-orbit coupling up to second order in perturbation theory. The numbers in parenthesis indicate the degeneracy of the states. The full splitting is only shown for ground state. States are labeled by the irreducible representations of the point group corresponding to the distortion. Energy separations are not to scale. The full term splitting can be found in Low et al. [6].
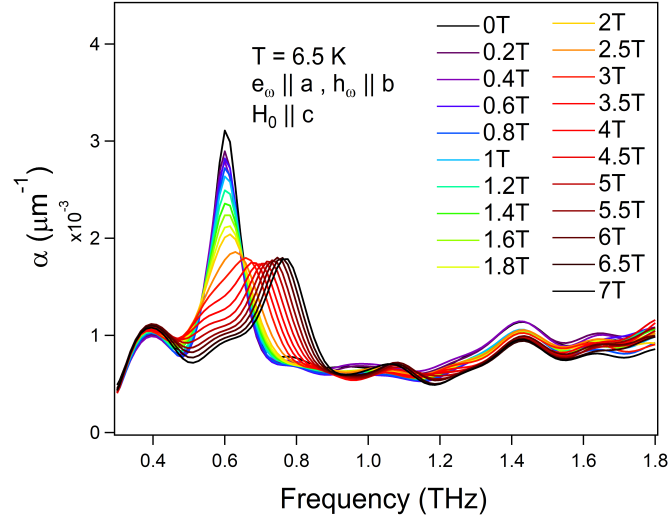
(a)
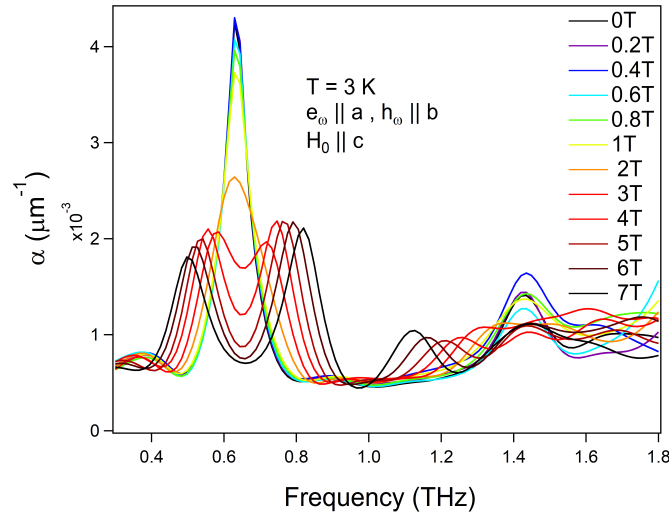
(b)

Figure 3.5: **THz measurement of the a-b plane in applied magnetic field H$_0$.** (a) At 6.5 K, in the paramagnetic phase, we observe the shifting in frequency of the α mode from 0.6 THz to 0.78 THz going from 0 to 7 T. The hump at 0.4 THz is believed to be an artifact of the Discrete Fourier Transform. Interestingly, the γ mode at 1.45 THz does not change with magnetic field. (b) At 3.0 K, in the antiferromagnetic phase, we see the clear splitting of the α mode. The field at which it completely split is between 1 and 2 T. The γ mode is seems to also split with increasing **H$_0$**. Due to low signal to noise ratio at higher frequencies, we can only say that at **H$_0$** causes γ to split into at least 2 modes, one remain unchanged with field, and one changes with field.

Chapter 4
ANTIFERROMAGNETIC MAGNONS IN $CaFe_2O_4$

4.1 Introduction

$CaFe_2O_4$ is a magnetic semiconductor with a bandgap of 1.9 eV [70, 71]. It has been subjected to a variety of studies due to its unique nature. Structurally, under high pressure, spinels tend to transform into the orthorhombic space group Pnma of ambient $CaFe_2O_4$ [72, 73]. From a semiconductor perspective, its bandgap makes $CaFe_2O_4$ an ideal photocathode material for water splitting [70, 71]. Extensive research efforts have also been spent on studying the magnetic properties of $CaFe_2O_4$ using neutron scattering [7, 74–76].

The magnetic ground state of $CaFe_2O_4$ was determined to be overall antiferromagnetic (AFM) below 200 K. The Fe^{3+} ions in assume the high spin configuration, resulting in an on site magnetic moment close to $4\mu_B$ pointing along the b axis [7, 74, 75]. The Fe^{3+} form ferromagnetic zig-zag chains along the crystalline b axis, with the chains antiferromagnetically aligned in the a-c plane [7]. Interestingly, previous neutron experiments showed multiple magnetic Bragg peaks with differing temperature dependences [7, 74, 75]. This observation indicates that there are two competing order parameters below the Neel temperature and the coexistence of two different microscopic magnetic phases. In the coexisting phases, weak ferromagnetic moment was found [76]. This is especially strange because the centrosymmetric crystalline structure would prevent canted antiferromagnetism from occurring.

High resolution inelastic neutron scattering work on $CaFe_2O_4$ revealed a hierarchy of

states at the magnon zone center [7]. This behavior is reminiscent of the bound states in the ferromagnetic Ising chain material $CoNb_2O_6$ [77, 78]. The difference in $CaFe_2O_4$ is that the discrete states were observed around the antiferromagnetic transition temperature of 200K, in comparison to the miliKelvin experiment in $CoNb_2O_6$. Stock et. al [7] put forth the idea that the discrete modes in $CaFe_2O_4$ come from the magnetic soliton-like excitations in the material.

One key ingredient believed to be the source of these phenomena is the anisotropic nature of $CaFe_2O_4$. Such anisotropy is evident in the exchange coupling constants, where $J_c/J_{ab} = 0.14$ [7]. Furthermore, it was found that the magnon excitation energy at its zone center, or $\mathbf{k} = 0$ is non-zero, in zero applied static magnetic field. This uniaxial energy gap was measured to be roughly around 3 meV (0.725THz) [7]. Such behavior can be explained by the crystalline or single-ion anisotropy of the material [35]. Upon further inspection, one would expect the orthorhombic crystal structure of $CaFe_2O_4$ to modify the zone center magnon excitation beyond the uniaxial case [35]. To take into account the orthorhombicity of the system, we can write the total spin energy as

$$
\begin{aligned}
E = \sum_{<i,j>} J_{ij}\mathbf{S}_i \cdot \mathbf{S}_j &- \frac{K_x}{2}\sum_i (S_i^x)^2 - \frac{K_y}{2}\sum_i (S_i^y)^2 \\
&- \frac{K_z}{2}\sum_i (S_i^z)^2 - g\mu_{\mathrm{B}}\mathbf{H} \cdot \sum_i \mathbf{S}_i
\end{aligned}
\tag{4.1}
$$

Where J_{ij} represents the exchange coupling constants along different bonds between the Fe ions, and K_x, K_y, K_z are the anisotropy constants along the crystallographic directions. In our experiment, we report the $\mathbf{k} = 0$ excitations of the spin wave modes in $CaFe_2O_4$ using THz spectroscopy. The momentum transfer from each photon relative to the magnon momentum is approximately zero.

We found that these excitation are anisotropic within the plane perpendicular to the easy axis, and thus consistent with the orthorhombic crystal structure. The prediction from a mean field spin wave theory agrees qualitatively with our data [35].

4.2 Experiment and Analysis Details

We performed the experiment in our home-built time-domain THz spectrometer. The spectrometer can be used with a Janis closed-cycled cryostat with optical access or an Oxford Spectromag, a liquid helium cryostat with a 7 T magnet. The sample was placed in each cryostat for the transmission measurements, with and without magnetic field. To obtain the transmission function $T(\omega)$ of the sample (4.2), we divided the spectrum of the THz pulse that passed through the sample by a reference. The reference spectrum, E_{ref}, is an identical measurement but without the sample in the THz beam path. The signal to noise of our instrument allows us to repeatably measure the response function between 0.2 and 2 THz. Each transmission measurement was done at constant temperature and magnetic field.

$$T(\omega) = \frac{E_{sample}(\omega)}{E_{ref}(\omega)} \tag{4.2}$$

Our sample was grown by floating-zone method, from the same group in these publications [7, 76]. The sample is approximately 573 microns thick, with the b axis perpendicular to the parallel surfaces. A pair of wire grid polarizers were used to determine the direction of the a and c axis. By aligning the polarization of the THz with the crystal axes, we can determine the selection rules of the spin wave excitations.

Since our transmission measurements only yield $T(\omega)$, further refinement is necessary in order to obtain the material's response functions $\epsilon(\omega)$ and $\mu(\omega)$. Equation (4.3) can be derived by writing down the propagation of a plane wave through a slab of thickness L. Here, ϵ, μ, c and ω are the permittivity, permeability, speed of light and angular frequency. It should be noted that some electromagnetism textbooks implicitly make the assumption that $\mu = 1$ at finite frequencies. Following the discussion about the dispersion of $\mu(\omega)$ in Landau, Lifshitz [29] sect. 79, we came to the conclusion that the value of μ should be close to unity in our experiment. The reason behind this is the fact that the wavelength $(0.03mm)$ is an order of magnitude smaller than the sample size $(0.5mm)$. As noted in the textbook, this does not simply mean $\mu = 1$, but it means that the macroscopic magnetic moment that we can measure would have a large contribution from $d\mathbf{P}/dt$. Hence, it would be an over-

refinement to distinguish **B** and **H** [29]. Although this assumption holds for wavelengths comparable or smaller that the dimension of the material, it breaks down around magnetic resonant frequencies, where the imaginary part of the magnetic susceptibility diverges or becomes quite large, depending on the damping of the system.

$$T = t_{1,2}t_{2,1}\exp^{i\frac{\omega}{c}L(\sqrt{\epsilon_2\mu_2}-\sqrt{\epsilon_1\mu_1})} \tag{4.3}$$

$$t_{1,2} = \frac{2}{\sqrt{\frac{\mu_1\epsilon_2}{\mu_2\epsilon_1}}+1} \tag{4.4}$$

$$\mu(\omega) = 1 + \frac{W}{(\omega_0^2 - \omega^2) + i\omega\Gamma} \tag{4.5}$$

The resonances for ϵ and μ can be modeled as Lorentz oscillators [12]. The complex response functions for these oscillators obey the Kramers-Kronig relations. We model ϵ with two Lorentz oscillators, one to emulate the strong phonon absorption above our spectrometer's bandwidth, and one weaker absorption at 1.4 THz. We made the assumption that at frequencies higher than the magnetic resonance, $\mu = 1$. Fitting the data above 1 THz using this model allows us to extrapolate the value of ϵ to lower frequencies. Once we have ϵ, we can numerically solve for μ around the magnetic resonance, using equation (4.3) and (4.4). Once $\mu(\omega)$ has been extracted, we fit it with equation (4.5).

4.3 Results

From the transmission plots in Fig. 5.2, we can see two strong absorptions around 0.62 THz and 0.73 THz at low temperatures, for $\mathbf{h}_\omega||\mathbf{a}$ and $\mathbf{h}_\omega||\mathbf{c}$ respectively. These absorption frequencies are at approximately the same energy as the magnon energy gap reported in the previous neutron scattering study [7]. We would like to note that the neutron experiment did not report two different anisotropic magnon gaps. The line shape of the absorptions around 0.6-0.7 THz is not symmetric, in both orientations. This could be the result of its interference with a broad absorption feature just below 0.5 THz. This broad feature could possibly be the so called "orphan spin" excitation reported in another neutron scattering

work [76].

One notable difference between the two polarization measurements is an absorption at 1.6 THz, which is only present when $h_\omega||a$ (and $e_\omega||c$). Its strength is much weaker than the absorptions below 1 THz. Another weaker absorption feature can be seen in the $h_\omega||c$ configuration around 0.84 THz. These features are very likely related to the magnetic phase as we only observe them at lower temperatures. We believe that the overall slope at higher temperatures is the tail of a phonon at frequencies above our bandwidth. It is expected for a phonon frequency width to increase and its center frequency to lower as temperature increases.

After the extrapolation of ϵ and calculation of μ, we can clearly see that the strong absorption seen in the transmission is indeed associated with the magnetic phase, see Fig. 5.3. The resonant frequency is redshifted to lower frequencies as the temperature increases up to $T_{Neel} \approx 200K$. The resonance disappears completely above T_N. The results of fitting μ with (4.5) can be seen in Fig. 5.5. The resonant frequencies are unique in each polarization configuration up to near T_N, where they became too weak to resolve. The temperature dependence of the oscillator strengths can be seen in comparison with the ordering parameter measured in [7] in Fig. 5.6. It can be seen that the magnons measured with our THz experiment are associated with the magnetic B-phase.

Another interesting behavior can be seen at low temperature, where there is a sharpening of the resonance width around 30-40K. The resonance width follows the typical behavior of thermal broadening at higher temperature as we approaches T_N. Above 160K, the feature that we have been following becomes comparable to the background. Without prior knowledge of the background, the fitting procedure cannot differentiate between the two.

In an applied static magnetic field, $\mathbf{H_0}||\mathbf{b}$, we observed the frequency shifting of the two modes previously observed 4.7. These modes at zero field move in opposite directions to one another. At about 1 Tesla, there appear another absorption mode in each measurement configuration. These new modes also shift in frequency with increasing field, and they move away from the original mode. Upon closer inspection, we notice that the frequency of these 4 modes at high magnetic field are not unique. It appears that the higher frequency

absorptions (in different configurations) are degenerate in energy. The same applies to the lower frequency absorptions.

4.4 Discussions

We can qualitatively explain our data using symmetry. One would expect an isotropic Heisenberg antiferromagnet to have no energy gap at the magnon zone center [10]. In other words, it takes a zero energy to create an excitation where the spins are changing uniformly in space. By breaking the rotational invariant symmetry of such a system, we should expect to create an energy gap. An example of the consequence of such symmetry breaking can be observed by applying a static magnetic field. Since there is a unique direction where the spins would prefer to align, it takes a finite amount of energy, precisely the Zeeman energy in this case, to create a uniform excitation. An uniaxial anisotropy that arisen from spin-orbit coupling and crystallographic distortion can also achieve the same effect. One should expect an orthorhombic anisotropy, where there are multiple unique axes, to have a more complex effect on the energy gap.

An of interesting behavior emerged from fitting these absorption with a Lorentz oscillator. The oscillator is not able to capture the of resonant ringing or asymmetry of actual data. The fits are consistently under-fitting the lower frequency portion of the resonance. It is apparent in our transmission data that the resonances are not symmetric (Fig. 4.2). Asymmetric line shape (called Fano line shape) can be explained by the coupling between a sharp resonance (AFM magnon) and some broad feature. This suggests that the magnon is coupling to an underlying broad feature at low frequencies. In fact inelastic neutron scattering have observed a broad scattering intensity inside the magnon gap [76]. This is argued to be caused by the excess of magnetic moments due to the antiphase boundaries. These moments are not compensated, and hence form a net magnetization. The broad scattering feature is the excitation of these so called "orphan spins".

We turn our attention to the description of $CaFe_2O_4$ using spin wave theory. Keffer and Kittel have worked out the problem of the antiferromagnetic spin wave with orthorhombic

anisotropy [35]. This work ignored the microscopic spin configuration, but instead used two mean-field magnetization sublattices, antiferromagnetically coupled to one another. The spin waves resulted from applying the Landau-Lifshitz-Gilbert equation are two distinct eigen-modes even with zero static magnetic field. By calculating the susceptibility, Keffer and Kittel determined that each mode is only accessible when the oscillating magnetic field is oriented at a particular crystalline direction. The experimental data that we have observed is consistent with this theory.

We next try to explain our observations of the spin waves in the framework of the measured magnetic structure in [7, 74, 75]. The spin structures found by neutron scattering are shown in Fig. 4.5. At low temperature, there are two coexisting magnetic Bragg peaks, implying two different spin structures, labeled A-phase and B-phase. The inelastic neutron data from [7] revealed the weak exchange coupling along the crystalline c-axis. This effectively means that spins in $CaFe_2O_4$ form a-b layers with intralayer antiferromagnetic exchange interactions and a relatively weak interlayer coupling, which is ferromagnetic in the A-phase and antiferromagnetic in the B-phase. Due to the weak interlayer coupling, we should note that the A and B-phase magnons are expected to be nearly degenerate, making their detection challenging with our instrument's resolution.

The model (4.1) was used to calculate the magnon excitation spectrum in $CaFe_2O_4$. The dynamic response of each phase due to an AC magnetic field, $\mathbf{h_i} = \mathbf{h_0}\ e^{-i(\omega t + \mathbf{q} \cdot \mathbf{x}_i)}$, is calculated numerically using the Landau-Lifshitz-Gilbert (LLG) equation. The calculated magnon dispersion 4.6 is used to fit with data from our THz experiment and neutron scattering experiment. We found that $J_1 = 7.025 meV$ and $J_2 = 0.219 J_1$. The coupling J_3 is much weaker and ferromagnetic in the A-phase: $J_3 = -0.004 J_1$. Furthermore, the values of the anisotropies terms are: $K_z - K_x = 0.006 J_1$ and $K_y - K_x = 0.0015 J_1$. The Gilbert damping is found to be $\alpha = 0.0031$ from fitting our THz resonance data. The calculated ratio of the absorption spectral weights for the two directions of the THz magnetic field, $h_\omega || a$ and $h_\omega || c$, is 1.12 and in good agreement with 1.25 from the THz data at low temperatures.

By ignoring the weak J_3 coupling and considering an effective chain model with two antiferromagnetic sublattices and exchange constants $2J_1$ and $2J_2$, we can gain more insight

into the nature of the antiferromagnetic magnon modes. Using the LLG equation, we can calculate the antiferromagnetic resonance frequencies for each spin chain in zero applied magnetic field:

$$\omega_1 = S\sqrt{4(J_1 + J_2)(K_z - K_y)} \tag{4.6}$$

$$\omega_2 = S\sqrt{4(J_1 + J_2)(K_z - K_x)} \tag{4.7}$$

Through the calculated the directional dependence of the magnetic susceptibility, we confirm that each spin wave mode can be selectively excited by aligning the THz magnetic field along the a-axis or the c-axis. The frequency splitting, $\omega_1 - \omega_2$, originates from the difference in anisotropies, K_x and K_y, along the two crystallographic directions. This result is again consistent with the result from Keffer and Kittel [35] where they only considered two mean-field magnetization sublattices with no details on the magnetic structure. Applying a static magnetic field along the crystalline b-axis, the preferred direction of the spins, we also confirm that the frequency splitting increases and ω_1 and ω_2 become excitable by an incident THz magnetic field of any direction within the a-c plane (Fig. 4.7).

4.5 Summary

In summary, we present the magnon zone center measurement using polarized THz spectroscopy. We observed multiple strong absorption at zero static magnetic field. These can be thought of as different uniform excitations of an antiferromagnet with orthorhombic anisotropy. A spin full classical spin wave calculation revealed that the two modes observed are indeed coming from the orthorhombic anisotropy term in our Hamiltonian. The temperature dependence of the observed excitation implies that it is associated with only the magnetic B-phase, reported in [7]. Our calculation also confirm the selection rules in the zero static magnetic field measurement and also when we apply a magnetic field.
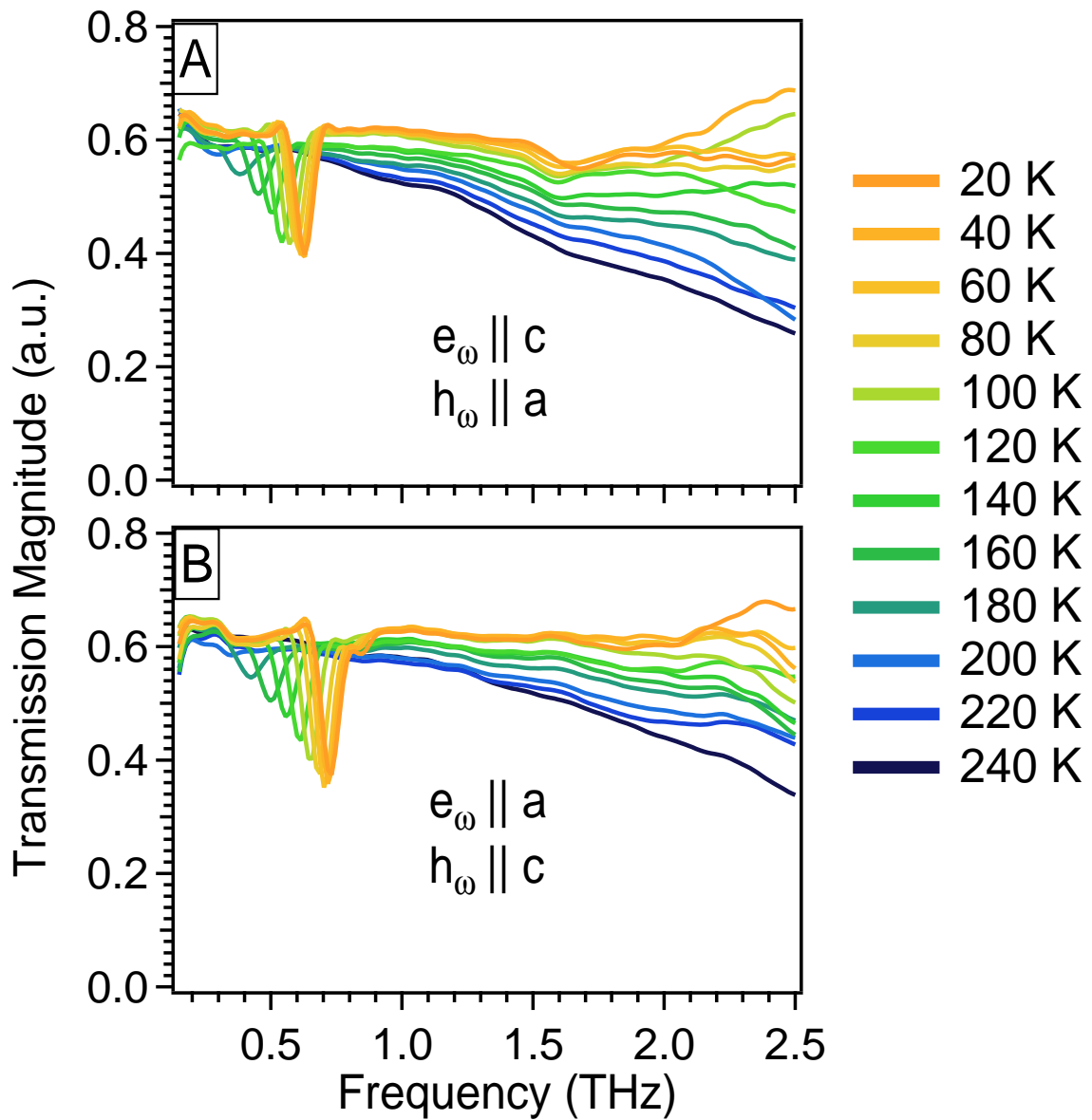
Figure 4.1: **Magnitude of transmission function**. Transmission of THz radiation through b-cut sample (A) $h_\omega || a$ (B) $h_\omega || c$. A resonance around 0.6 THz that changes with temperature can be seen in each measurement configuration. A small difference between the the center frequency of these resonances can be seen. A weaker resonance around 1.6 THz can be seen. The signal to noise ratio makes it difficult to track its temperature dependence.
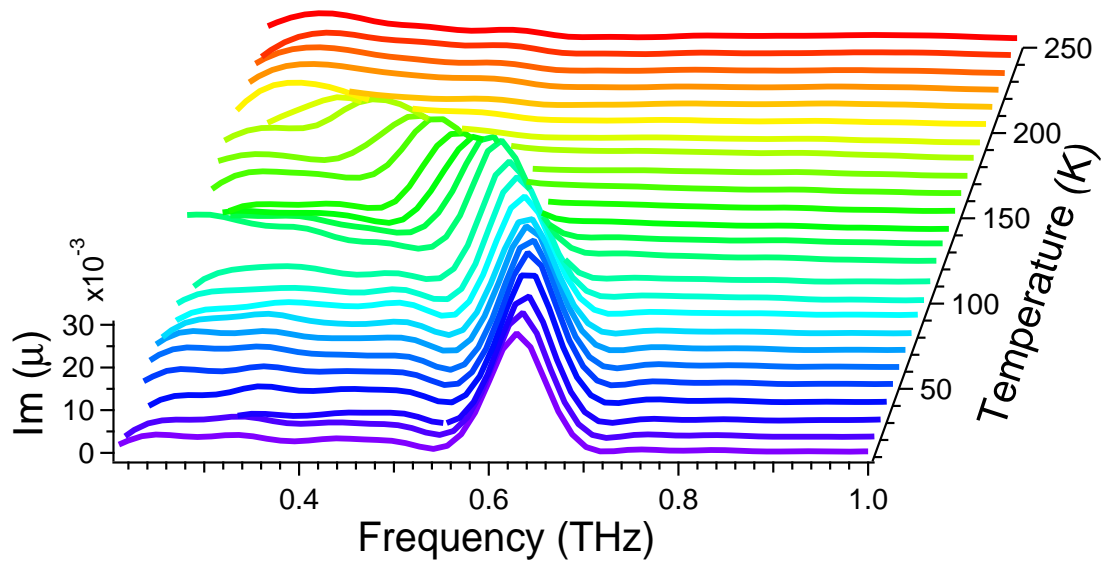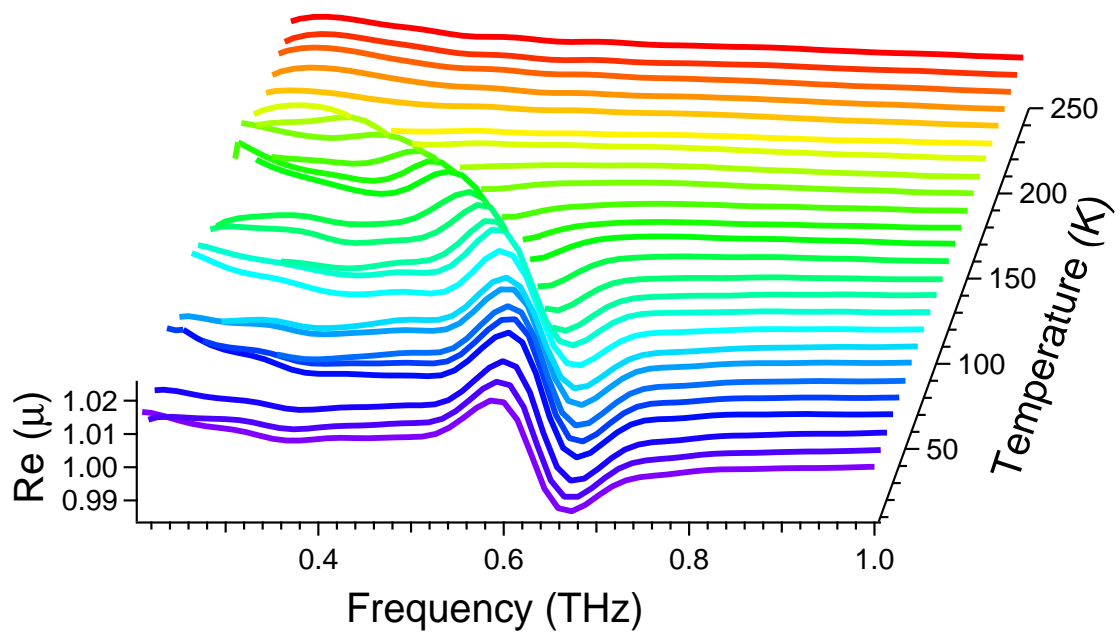
Figure 4.2: **Magnetic Response**. Real and imaginary parts of the magnetic response of CaFe$_2$O$_4$ in the THz frequencies as a function of temperature for $h_\omega || a$. We can clearly see the appearance of the magnetic resonance below T_N
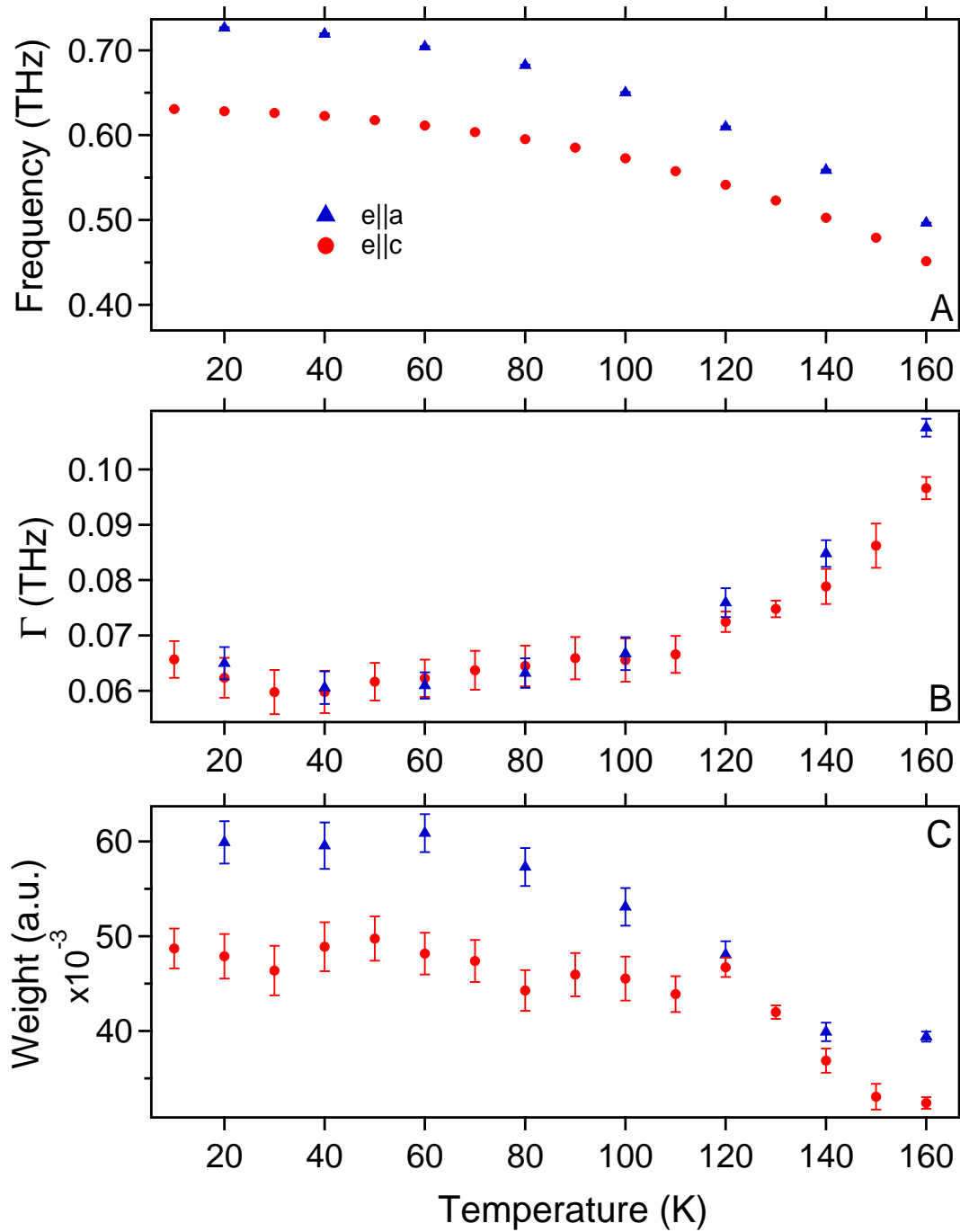
Figure 4.3: **Lorentzian fitting result**. Property of the oscillator as a function of temperature, (A) resonant frequency, (B) width of resonance, (C) strength of oscillator
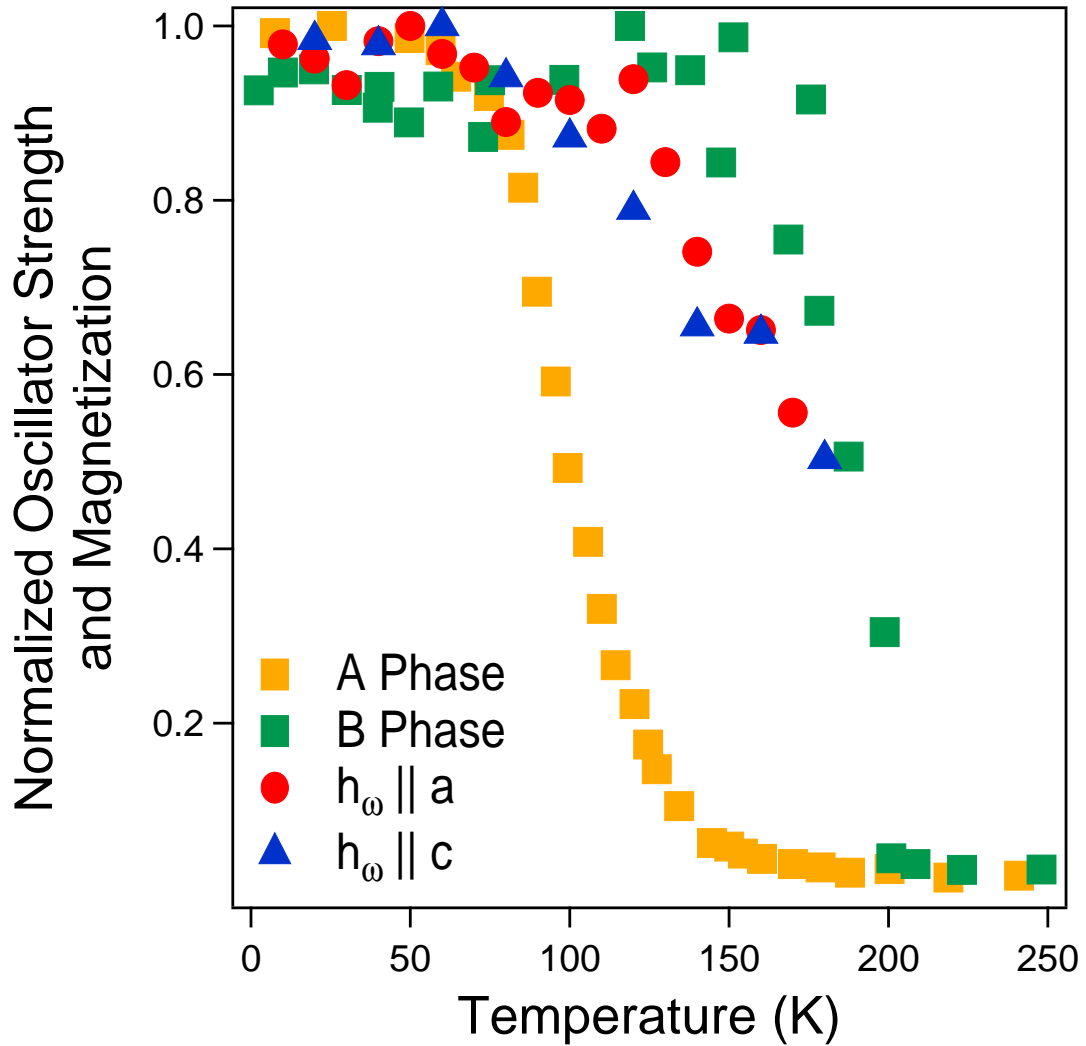
Figure 4.4: **Normalized Spectral Weight**. Comparison of the fitting results with magnetic moments from [7].The spectral weights are normalized to their maximum values, the moments are also normalized to their maximum values. We can clearly see that the two magnons observed with THz spectroscopy is associate with the magnetic B-phase.
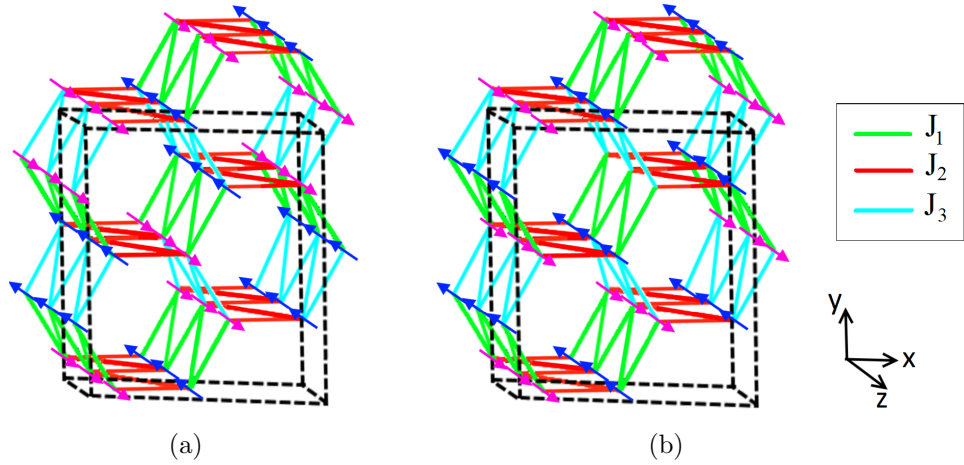
Figure 4.5: Magnetic orders in the A- and B-phases (panels (a) and (b), respectively). Arrows represent spins aligned parallel or antiparallel to the z axis. Bonds with three different exchange constants are indicated by red, green and cyan color.
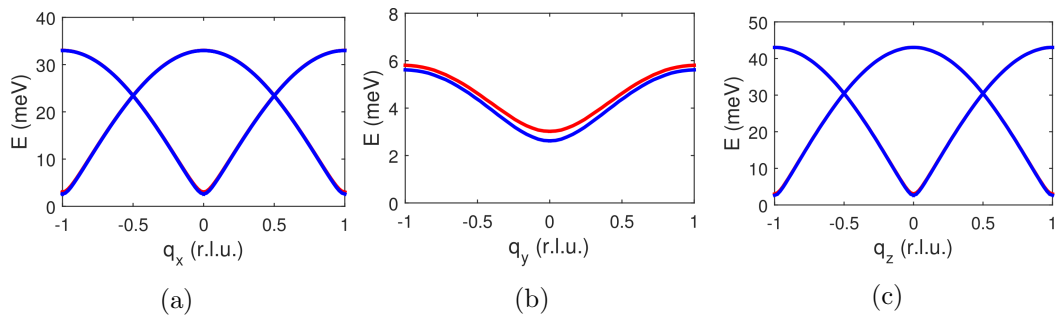
Figure 4.6: Numerically calculated magnon spectrum for the wave vector (a) $q \parallel x$, (b) $q \parallel b$ and (c) $q \parallel z$. Blue (red) line is for magnons excited by the ac magnetic field $h \parallel x$ ($h \parallel y$).
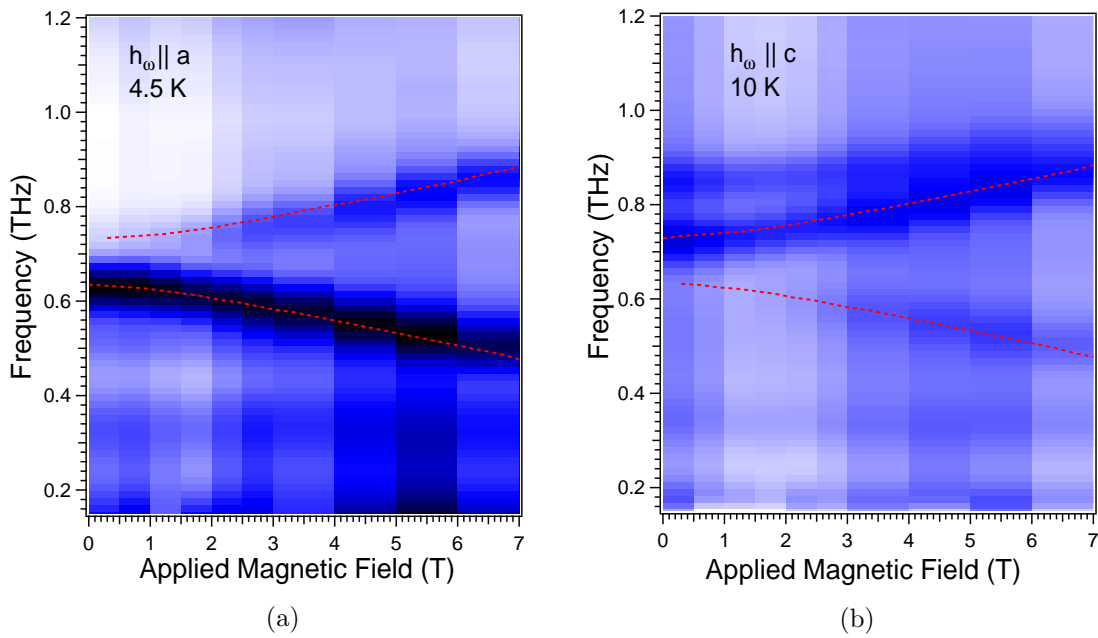
Figure 4.7: Magnetic field dependence of the THz absorption spectra. The two AFMR modes measured in magnetic field are compared to numerically calculated resonances(red dash) at $T = 4.5$ K and $T = 10$ K for $h_\omega \parallel a$ and $h_\omega \parallel c$ respectively. This confirms the breaking down of the selection rule as a static magnetic field is applied along the b-axis

Chapter 5
α-RuCL$_3$

5.1 Introduction

Quantum spin liquid (QSL) is a thriving area of research in condensed matter physics. This ground state of matter is of interest due to its quantum mechanical nature and exhibit exotic behaviors [79]. In typical magnetic crystals, the magnetic moments exhibit long range correlation (the size of a sample, or at the very least μms size domains). These moments could either prefer to point parallel to one another or antiparallel to its neighbors. These two simple pictures represent ferromagnetic ordering and antiferromagnetic ordering. The details are typically much more complicated as these magnetic moments live on different crystalline lattices.

Let's consider a 2-D square lattice, with a spin on each of the vertices 5.1. If the other factors from the system (atomic orbitals overlap, hopping, etc.) impose that each spin must align antiferromagnetically with each other (closest distance neighbor). We would have a simple ground state as seen in Fig. 5.1. Let's consider a different 2-D lattice, a triangular one. Let's assume that the system also imposes an AFM nearest neighbor coupling. There is no "good" way to align the spins that would satisfy the AFM coupling requirement. This is a simple picture of geometric frustration. A similar situation exists in many 3-D crystal lattices. The ground state of such frustration can be a QSL. What it means is at zero Kelvin, the spins are not nicely aligned like the square lattice, but the ground state is a superposition of multiple configurations.

There are more rigorous definitions of a QSL, however, an intuition can be obtain
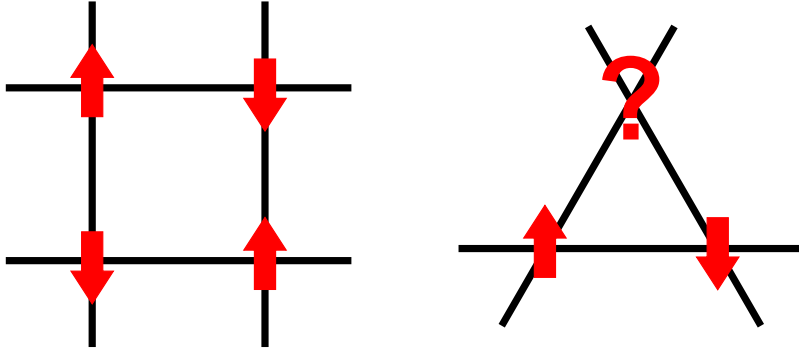
Figure 5.1: **Geometric frustration in 2D triangular spin lattice**. A simple picture of 2D square and triangular lattice, with spins (red arrows). If the constraint is such that nearest neighbor sites have opposite spins, the square lattice can easily fulfill this condition. However, the triangular cannot. As a consequence, the third spin can be either up and down, leaving a degeneracy in the system. Such degeneracy prevents the spins on this lattice from ordering.

by thinking about the classical liquid. In a solid, all the "molecules" have long range correlation. The meaning is that there is a definite relationship between the location of two atoms across a large distance (infinity if we consider a perfect crystal at zero temperature and no quantum fluctuation). In a liquid, like water, the molecules have no long range correlation. However, at short range, there is correlation between adjacent molecules. The short range correlation typically comes from the interaction between the adjacent molecules, while thermal fluctuation is the cause of the lost in long range order. In a QSL, there is short range correlation between the spins, but the long range order has been destroyed by quantum fluctuations (quantum mechanical fluctuations as oppose to thermal fluctuation).

In a real material, the crystal lattice often distorts itself to relieve this frustration. α-RuCl$_3$ is a candidate for the Kitaev model [80, 81]. This model is characterized by 3 independent bonds. The magnetic ground state of this model is a QSL. However, it

59

was found that α-RuCl$_3$ orders antiferromagnetic below ~ 6 K [82, 83]. The bulk crystal symmetry of α-RuCl$_3$ is $C2/m$ [82, 83]. The **a-b** plane can be characterized by quasi-honeycomb layers monoclinically stacked along the **c** axis (Fig. 5.2). The **c** axis makes approximately $108°$ angle with the **a** axis. This monoclinic stacking was found to repeat every 2 layers (AB stacking). Van der Waals coupling weakly hold each 2-D layer together. The monoclinic stacking breaks the C_3 symmetry of each layer, leaving C$_2$ as the highest symmetry remaining in the bulk. The special two-fold symmetry axis is in the plane and along a Ru-Ru bond. Refinement of diffraction data from previous studies revealed a small distortion of one of these bonds (out of 3), in the order of ~ 0.01 Angstrom. This distortion is possibly the relief mechanism for the magnetic frustration.

Although long range magnetic ordering does occur in α-RuCl$_3$, inelastic neutron scattering (INS) revealed hints on QSL physics in this material [84, 85]. A magnon gap was measured by both INS and optical spectroscopy, along with a broad scattering continuum. Fractionalized spin excitations is the proposed explanation to the continuum. Typical spin excitations have $\Delta m_s = 1$, while fractionalized spin excitation would have $\Delta m_s = 1/2$. The details of this excitation lie in the heart of QSL physics and is beyond the scope of this study [81]. However, an immediate consequence of such exotic QSL behavior should be recognized. The difference between these two magnetic excitations: a bosonic ($\Delta m_s = 1$) vs. fermionic ($\Delta m_s = 1/2$) excitation. They obey different statistics. THz spectroscopy measurements have also seen a broad magnetic excitation, similar to one by inelastic neutron scattering [86–88].

Previous Raman studies of α-RuCl$_3$ have focused on the broad magnetic scattering continuum and its relation to the Kitaev model [8, 89, 90]. Most of the publications use the symmetry of α-RuCl$_3$'s perfect honeycomb layer. Specifically, the observed scattering continuum has been propose to be the same as the predicted Kitaev scattering continuum in the layered irridate [91], with E_g symmetry. We set out to study the effects of symmetry breaking on α-RuCl$_3$'s phonon spectrum as a whole and more specifically the scattering continuum.
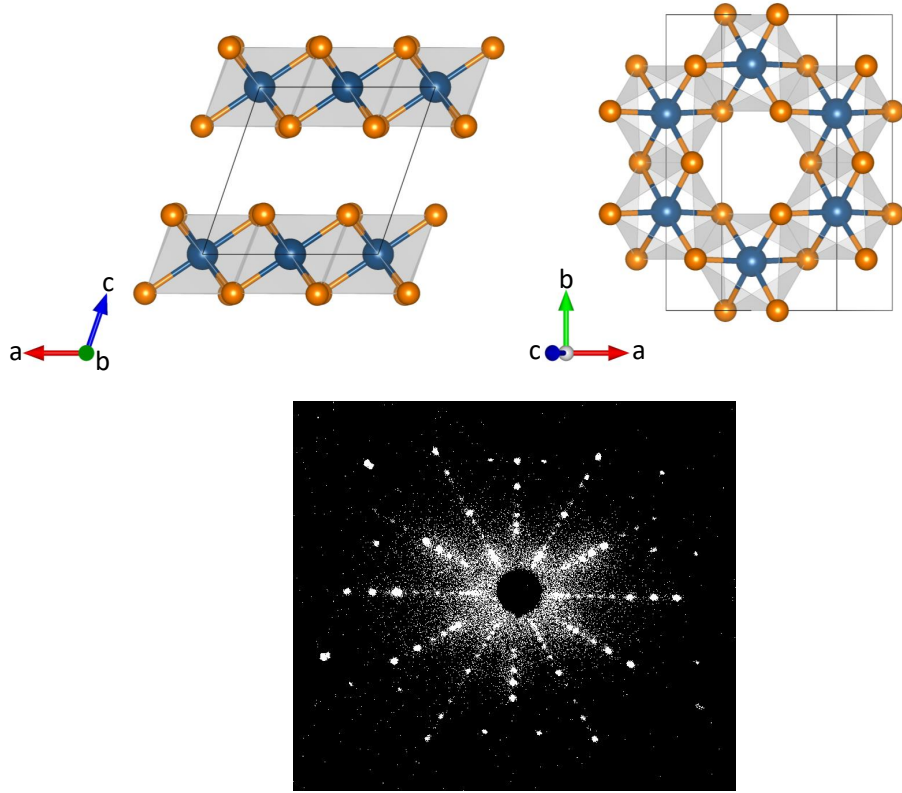
Figure 5.2: **Crystal structure and Laue X-ray diffraction pattern**. Crystal structure of α-RuCl$_3$ projected onto the **a-b** and **a-c** plane. The solid black lines represent the unit cell. The orange balls represent Cl atoms, while the larger blue balls represent Ru atoms. Typical Laue diffraction pattern of the **a-b** plane. The pattern remained unchanged over many millimeters.

5.2 Experiment

Our sample is grown by the same group in these studies [82, 84, 85]. Laue diffraction patterns were taken on the surface of the sample (layering plane) to confirm the large domain single crystal nature of our sample (Fig 5.2). Raman spectra for 514.5308 nm laser excitation were measured in ambient conditions using a single-grating spectrometer (Renishaw inVia micro-Raman, 1800 lines/mm grating, 1.27 cm CCD detector) in the 180° backscattering configuration. A combination of half wave plates and linear polarizers were used to measure phonons in either parallel or crossed polarization configurations, where

the polarization orientations were confirmed using MoS_2 as a reference sample. The α-$RuCl_3$ sample, where the **a** and **b** axes were known from Laue diffraction, was placed on a rotator stage to probe different crystal orientations. To probe the a-c plane, the α-$RuCl_3$ was mounted on its side and a long working distance objective was used to focus on the m̃m thick side of the sample. Integration times ranged between 5 minutes (a-b plane) and 12 minutes (a-c plane), and the laser power was kept below 200 μm through the objective (50x, Numerical Aperture 0.75 to probe a-b plane, 100x long working distance objective, Numerical Aperture 0.75 to probe a-c plane) to avoid any local heating of the sample.

The point group symmetry of the bulk crystal is $2/m$ (or C_{2h}). One would expect the Raman response tensor to have the form shown in equation 5.1. It should be pointed out that the crystallographic b-axis is the high symmetry axis and is identically the tensor y-axis. We expect to observe 12 Raman active phonons $6A_g + 6B_g$ in this point group. The selection rule allows for both A_g and B_g phonons to be measured in our measurement of the **a-b** plane. In contrast, the **a-c** plane should only show A_g phonons. We expect the intensity of the A_g phonon to be out of phase with B_g as the polarization angle changes within the **a-b** plane.

Our experiment can be described by using the Raman response tensor predicted by group theory.

$$A_g = \begin{bmatrix} a & 0 & d \\ 0 & b & 0 \\ d & 0 & c \end{bmatrix} ; B_g = \begin{bmatrix} 0 & e & 0 \\ e & 0 & f \\ 0 & f & 0 \end{bmatrix} \tag{5.1}$$

5.3 Results

Through the help of X-ray Laue diffraction, we determined the crystalline **b** axis of our sample (Fig. 5.2). With the **a-b** plane defined as the van der Waals layers plane, we can uniquely determine the other crystal axes. The initial result of the **a-b** plane taken with incoming polarization parallel to **b** is presented in Fig. 5.3. We observed

		Parallel	Crossed
a-b	A_g	$(a+b)+(a-b)\cos(2\theta)$	$(b-a)\sin(2\theta)$
	B_g	$e\sin(2\theta)$	$e\cos(2\theta)$
a-c	A_g	$(a+c)+(a-c)\cos(2\theta)-2d\sin(2\theta)$	$(a-c)\sin(2\theta)-2d\cos(2\theta)$
	B_g	N.A.	N.A.

Table 5.1: **Raman Angular Response of the a-b an a-c plane of α-RuCl$_3$** Derived from Raman tensor in Eq. 5.1. Here, the crystalline **b** axis is identically the tensor y-axis, and **a** is the x-axis, while **c** is *not* the z-axis.

similar spectra as previous Raman studies on α-RuCl$_3$ [8, 89]. Upon closer inspection, we can see small differences in the phonon frequencies between the crossed and parallel configuration, particularly around 164 cm^{-1}, 270 cm^{-1}, and 295 cm^{-1}. These differences are approximately 2 cm^{-1}. In addition, the weaker phonon peak at 118 cm^{-1} seems to have an additional peak in the parallel configuration. It should be noted that previous studies did not point out these subtle changes between the crossed and parallel configurations. They have either assumed that these are the same phonon in [89, 90], or underestimated the frequency difference (sub cm^{-1}) [8]. The phonons in our spectra have been labeled with the irreducible representations A_g and B_g of the point group 2/m (C$_{2h}$) in Table 5.2, which is the point group symmetry of bulk α-RuCl$_3$.

Our room temperature measurements also show the asymmetric phonon peak at 164 cm^{-1} (Fig. 5.3), which is consistent with other publications[8, 89]. The asymmetric Fano lineshape typically arises when a discrete resonance, a phonon in this case, is coupled to a broad continuum[92]. It was conjectured that at low temperature, such scattering continuum is partially due to the magnetism of α-RuCl$_3$. Multiple authors have argued that this room temperature magnetic continuum has its root in the Kitaev physics [91, 93]. Quasielastic scattering (QES) has been proposed to be the largest contribution to the continuum at room temperature. We would like to point out that THz transmission was reported through $\sim$mm thick single crystal α-RuCl$_3$ [86, 87]. Such measurement implicates that α-RuCl$_3$ is highly insulating. We would expect the free electron response to be negligible. It's

	$1^\dagger$	$2^\dagger$	3	$4^\dagger$	$5^\dagger$	6
A_g	119.4	164.2	222	271.9	295.8	313.1
B_g	115.8	165.8		269.3	297.6	291.5

Table 5.2: List of A_g and B_g phonons. The symmetry asignment of these phonons were determined by its intensity when the laser polarizations are on a crystalline axis (**a** or **b**). In such polarization configuration, A_g modes appear in parallel and B_g in crossed. The † here denotes pairs of nearly degenerate phonon modes.

important to point out that another candidate of the Kitaev magnet, β-Li$_2$IrO$_3$, exhibits a similar broad continuum along with multiple asymmetric phonons at room temperature [94].

$$I(\omega) = I_0 \frac{1}{(1+q^2)} \frac{(q + (\frac{\omega - \omega_0}{\Gamma}))^2}{1 + (\frac{\omega - \omega_0}{\Gamma})^2} \tag{5.2}$$

To determine the phonons resonant frequencies, we fitted each peak with a Lorentzian lineshape. The exceptions are the peaks around 164 cm^{-1} where we use the Fano line shape equation (Eq. 5.2) instead. Here, q represents the asymmetric parameter. A Lorentzian lineshape is recovered as q goes to infinity (or $1/|q| = 0$).

As the relative angle between the laser polarization and the crystalline axes changes, we observed the apparent oscillations in the phonon frequencies in both crossed and parallel configuration (Fig. 5.4). Each phonon frequency oscillation can be explained by a pair of A$_g$ and B$_g$ phonons. Each phonon in the pair changes its intensity as the orientation is rotated, out of phase with one another. This behavior would give rise to the observed oscillation. We employed a model that contains multiple phonons with frequencies fixed by the A_g and B_g phonon frequencies to fit our data (Fig. 5.5).

The results of our fitting procedure is consistent with the assumption of multiple phonons per oscillation. The spectral weight of each phonon follows what group theory has predicted, as seen in the **a-b** plane rows of Table 5.1. In the crossed configuration, the change in intensity of A_g is indeed out of phase with B_g, as predicted by *sin* and *cos* respectively. The 313.07 cm^{-1} A_g phonon shows little change in intensity in the parallel configuration

(Fig. 5.4). This implies its tensor components $a = b$. That would explain the lack of intensity in the crossed polarization as the $I_{A_g} \propto (a - b)$ in the crossed configuration. In contrast, an interesting behavior of the A_g phonons near 270 cm^{-1} and 295 cm^{-1} can be seen in the parallel configuration (Fig. 5.5). The four nearly equal lobes of A_g phonons in the parallel configuration indicate that the tensor components a and b are approximately equal in magnitude and opposite in sign (or π phase difference).

We found that the phonon peak at 164 cm^{-1} shows similar changes to the oscillation of the 270 cm^{-1} and 295 cm^{-1} as the polarization angle changes (Fig. 5.4). In the crossed configuration, there is a resemblance of the oscillation in the frequency of the maximum intensities of this peak. In the parallel configuration, the behavior is less simple. The maximum intensity also shows variations as the sample is rotated (Fig. 5.4). In an attempt to determine angular dependences of the A_g and B_g phonon near 164 cm^{-1}, we again used the Fano lineshape equation (Eq. 5.2).

We are unable to obtain a good fit between 146 cm^{-1} and 180 cm^{-1} with two Fano lineshape. We can only speculate that this is likely due to the two extra parameters q. Another complication might be coming from the change in the background/continuum as a function of polarization angle. With a single Fano lineshape, we are able to observe the frequency oscillation in the crossed configuration, with the maximum and minimum frequency of $\sim$ 164.2cm^{-1} and 165.8cm^{-1}. They are of A_g and B_g symmetry respectively. In the parallel configuration, the behavior of the Fano phonon peak is consistent with the changing in intensity of these A_g and B_g phonons (see Supp. Mat.) We determined $1/|q|$ to be 0.064 and 0.091 for the A_g and B_g mode respectively.

Our measurement of the **a-c** plane shows no oscillating phonon peak, which is consistent with group theory (see Supp. Mat.) Only A_g phonons are expected in this plane. The most interesting feature in our data can be seen around 164 cm^{-1} (Fig. 5.6). Fitting the Fano peak in the **a-c** plane revealed how the asymmetry parameter q changes. In the parallel polarizations configuration, we see that the linewidth of the phonon is almost symmetric around 90$°$ (see inset). This angle corresponds to when the laser polarizations are pointing perpendicular to the van der Waals layers. By comparison, the crossed configuration also

show changes the phonon lineshape's Fano parameter. Its $1/|q|$ value in this configuration approaches zero when one of the laser polarization point perpendicular to the **a-b** plane.

5.4   Discussion

Previous studies of α-RuCl$_3$ has analyzed the Raman phonon spectra using the point group symmetry of each distortionless honeycomb layer D_{3d} [89, 95]. Factor group analysis reveals that the $4E_g + 2A_{1g}$ Raman active phonons in such point group would transform into A_g and B_g phonons of the bulk crystal. Specifically, the doubly degenerate E_g phonons mode of the higher symmetry point group would split into the A_g and B_g modes of the lower symmetry point group. Our observation of the nearly degenerate A_g and B_g phonons indicates that they are indeed closely related to the E_g phonons of the distortionless individual 2-D layer.

The A_g phonons at 271.85 cm^{-1} and 295.79 cm^{-1} also show evidence of this transformation. Four prominent intensity lobes in the **a-b** plane (Fig. 5.5) was measured in the parallel configuration. We can see that the tensors components probed by this measurement has the form of: $(a+b) - (a-b)Cos(2\theta)$ (Table 5.1). The observation implies that $b \approx -a$. A quick lookup of the E_g phonon Raman response tensor in the point group D_{3d} reveals that $b = -a$. We believe that the pairs of phonons around 270 cm^{-1} and 295 cm^{-1} were originally E_g phonons of each honeycomb layer. In contrast, the A_g phonon at 313.07 cm^{-1} does not show any angular dependence in the parallel measurement of the **a-b** plane. This observation implies that its tensor is similar to the A_{1g} phonon from the D_{3d} point group, where $b = a$.

Similar behavior was calculated in CrI$_3$ [96], an isostructural material to α-RuCl$_3$. Density Functional Theory predicted that the energy differences between the A_g and B_g pairs of phonons come from the weak interlayer coupling. That would explain the small magnitude of the frequency differences that we have observed. However, we should also expect the distortion of each layer to play a similar role in the phonon spectra of these materials. The magnitude of such distortion is minute [82, 83], which could be as likely to split the degen-

eracy of the E_g mode. Further theoretical study is necessary to pinpoint the mechanisms responsible for our observed spectra.

We now turn our attention to the Fano peak around 164 cm^{-1}. We observed changes in $1/|q|$ in the **a-c** planes, where it seems to approach zero at angles corresponding to polarizations out of the van der Waals layer. Group theory tell us that there is an out of plane response, specifically due to tensor component c and d in eq. 5.1. The vanishing $1/|q|$ means that the tensor component c and d has little to almost no coupling to the broad continuum. Meanwhile, tensor components a and b couple significantly stronger to the continuum, as seen in the **a-b** plane.

It should be noted that as $1/|q|$ becomes close to vanishing in the parallel configuration, the continuum seems to also vanish (Fig. 5.6). It is important to realize, however, that the Raman signal around 164 cm^{-1} comes from the phonon and also the continuum. The frequency dependence of this continuum makes it difficult to decouple the two effects. Our observation of the out-of-plane polarization is consistent with the observation of another group [8].

There are two possible explanations for this observation. The simplest explanation is that both the continuum and the phonon that's coupled to it are directly excited via the Raman process. With this mechanism, our observation would imply that the continuum is not excitable out of the van der Waals plane. In turn, the phonon's coupling strength $1/|q|$ would also diminish as the the continuum diminishes. Another possibility is that the continuum is excited indirectly via its coupling to the phonon. As the coupling strength vanishes, we would expect the continuum to vanish as well.

Previous Raman studies have argued that the continuum at room temperature is coming from some bosonic and fermionic source. Some authors have claimed that the fermionic contribution at low temperature persists to above $T = 7.5J$ [93], where J is the isotropic Kitaev exchange constant and of the order of a few meV. According to this claim, we would expect to measure the Kitaev continuum at room temperature. Other authors from [8] dismissed the phononic contribution to this continuum entirely based on its disappearance in the out-of-plane measurement. From then on, the only other contribution is a magnetic

one. This latter claim is something that our work can shed light on.

The observation of the symmetric phonon lineshape out-of-plane with parallel polarizations indicates that the scattering continuum is not a phononic effect. The continuum is clearly a 2 dimensional effect. A previous study have sketched out the atomic motion of the mode at 164 cm^{-1} [8] as the out of phase motion of the Ru atoms in the **a-b** plane [8]. It is conceivable that this motion is coupled to some magnetic excitation via the strong spin-orbit coupling effect of Ru atoms.

Another key insight can be obtained by looking at the Raman tensors. We observed a similar change in the Fano parameter in the crossed polarization. We can say that whenever any polarization is perpendicular to the **a-b** plane, the Fano coupling becomes vanishingly small (Fig. 5.6. In term of point group symmetry, the continuum, or rather the coupling to the continuum, cannot be described by the point group C_{2h}. We expect an out-of-plane response from a mode with A_g symmetry 5.1. However, this is consistent with the E_g phonon symmetry of the point group D_{3d} (eq. 5.3), where an out of plane response is not expected.

$$
A_{1g} = \begin{bmatrix} a & 0 & 0 \\ 0 & a & 0 \\ 0 & 0 & b \end{bmatrix} ; E_{g,1} = \begin{bmatrix} c & 0 & 0 \\ 0 & -c & d \\ 0 & d & 0 \end{bmatrix} \tag{5.3}
$$

Previous experimental studies have used E_g to label this scattering continuum [89, 93]. We can only guess as to why this was used. On one hand, the the theoretical study was done for a perfect honeycomb layer with D_{3d} point group. While the initial experimental study drew inspiration from other studies on the layered honeycomb irridates (a 3D Kitaev system) [91]. Since then, there have been multiple theory publications on the 2D honeycomb system [97].

The Raman selection rule for magnetic scattering was derived for a single honeycomb layer [97]. For a spin Hamiltonian that only has nearest neighbor interaction, and all the interactions obey the crystal symmetry, the magnetic excitations have the E_g symmetry. Again, we expect an excitation with E_g symmetry to vanish out of the 2D plane 5.3. Our

observation of the vanishing Fano parameter out of plane is indicative of an E_g symmetry. This means that what we have measured is indeed magnetic in origin. We cannot say, however, that this magnetic scattering continuum is due to the Kitaev interaction. We can only say that nearest neighbor exchange is dominant, and symmetric under the crystal symmetry.

5.5 Summary

In summary, we measured the Raman phonon spectrum of α-RuCl$_3$ at room temperature and found it to be consistent with the point group C_{2h}. We found multiple links between these phonons to the point group D_{3d}, the symmetry of each perfect honeycomb layer. This observation is consistent with factor group analysis where the E_g phonons of D_{3d} become pairs of A_g and B_g phonons of C_{2h}. We also observed the Fano resonance near 164 cm^{-1} and found that it is made up of a pair of A_g and B_g phonons with different coupling parameters to the broad background/continuum. Our measurement with the laser polarization pointing out of the honeycomb layer is also consistent with the point group symmetry of the bulk crystal. An interesting observation was made where we see the coupling of the Fano resonance to be diminishing out of the **a-b** plane. This vanishing coupling suggests that the scattering continuum/background is of E_g symmetry. Comparing to the Raman magnetic scattering selection rule, we concluded that this background is of magnetic origin.
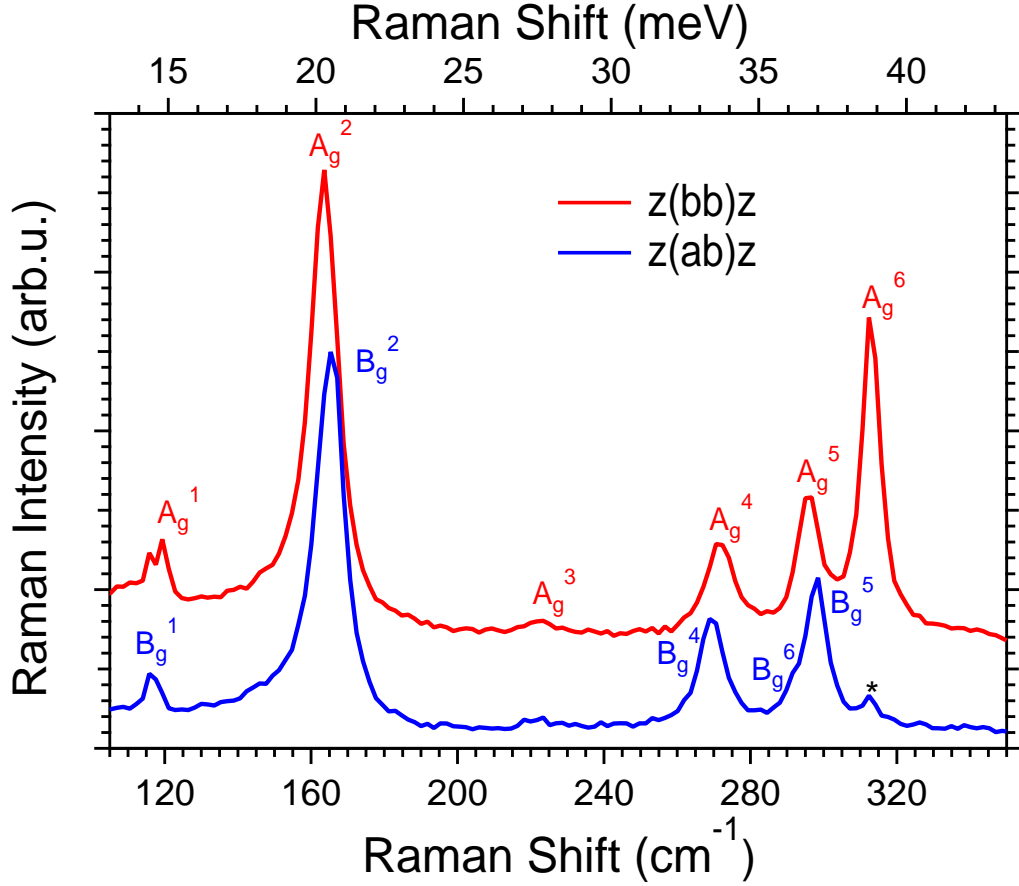
Figure 5.3: **Raman Intensity of a-b plane**. The parallel configuration plot is offset for clarity. The *Porto* notation is used for the polarization. Here **z** is the lab frame coordinate in which the incident and scattered beams propagate. **a** and **b** are the crystallographic axes. Clear difference between some of the phonon frequencies in the crossed and parallel configuration are observed. We labeled these phonons with A_g and B_g, of the bulk point group symmetry C_{2h}. The * mode seen in crossed is the A_g^6 phonon signal leakage due to our imperfect polarizers.
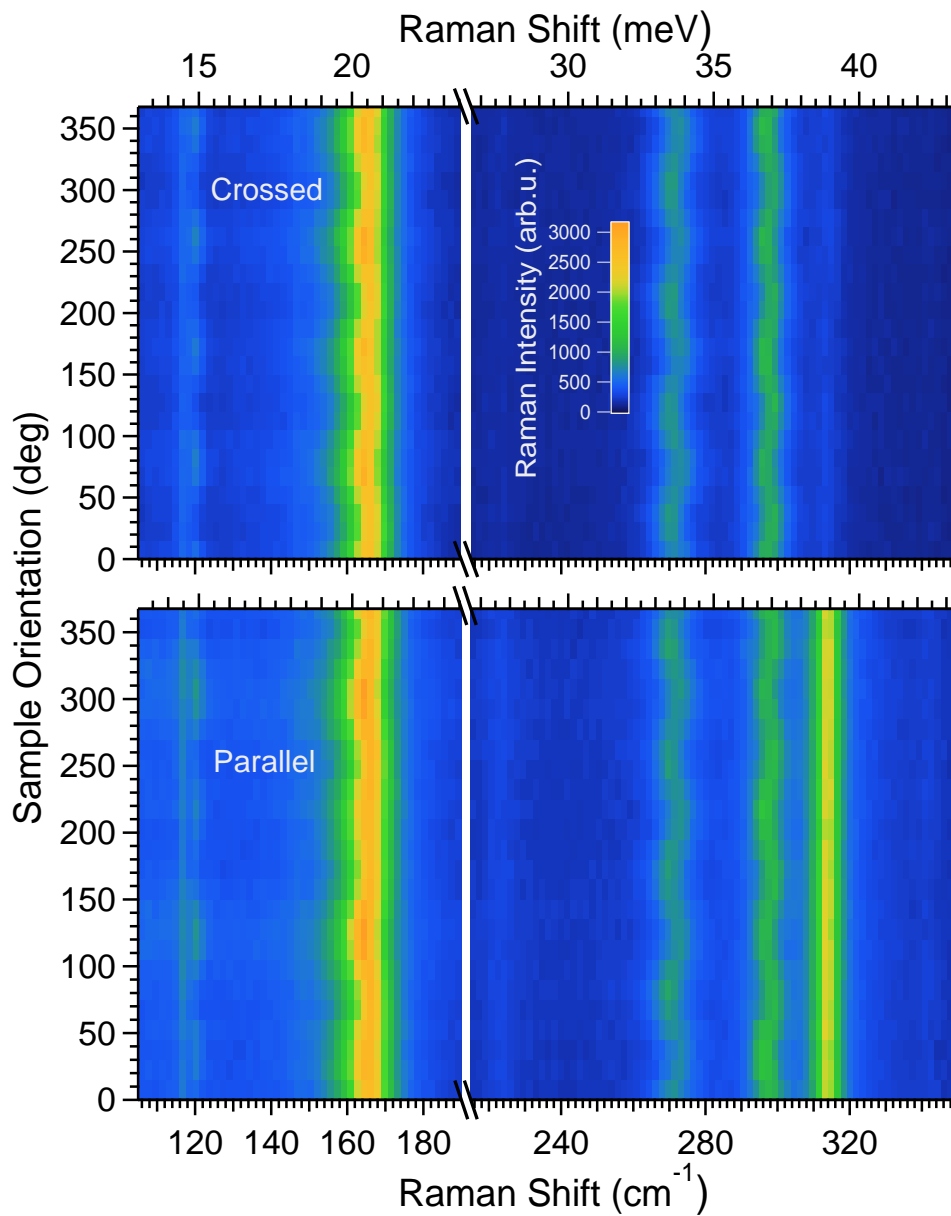
Figure 5.4: **Raman Intensity as a function of rotation angle of a-b plane**. Raman intensity as a function of frequency and sample orientation
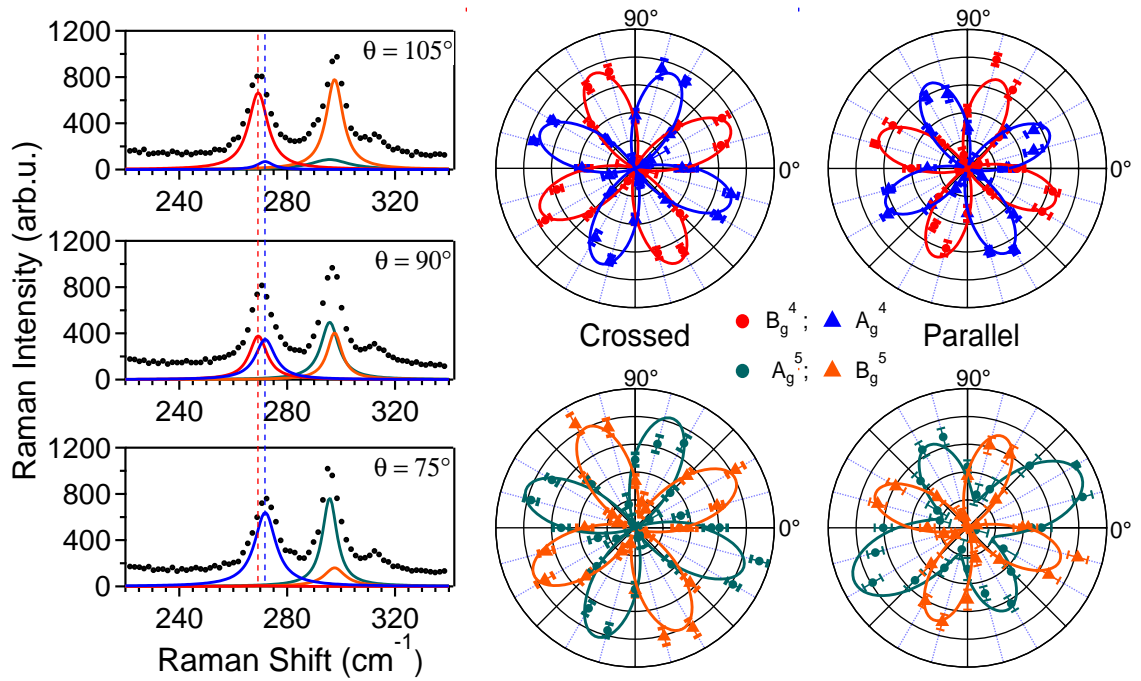
Figure 5.5: **Angular dependence of phonon spectral weights**. Each apparent oscillation is fitted with a pair of phonons. The spectral weight output is then fitted with equations from Table 5.1, shown by solid lines.
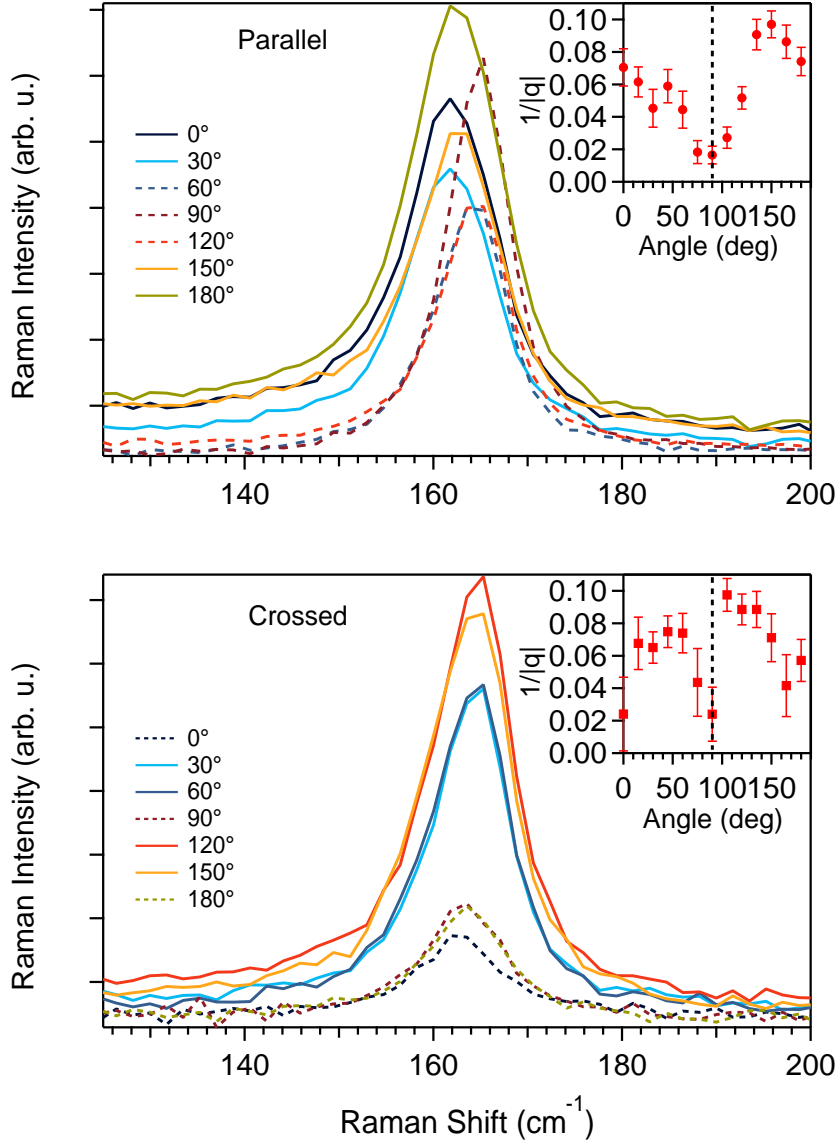
Figure 5.6: **Fano peak in the a-c plane**. In the parallel configuration, as the polarization points entirely perpendicular to the layer, the $164 cm^{-1}$ phonon seems to become nearly symmetric. A similar situation can be seen in the crossed polarization. The insets show the fitted Fano parameter q. We expect $1/q$ vanishes for a symmetric Lorentzian.

Chapter 6
SUMMARY

One of the key to understanding cooperative phenomena such as phonons and magnons is by the symmetry of the system that host these effects. The discrete translation and rotation symmetry of a crystal imposes strict symmetry on the quantum mechanical ground state of such system. Through the electromagnetic coupling, polarized light is not only able to probe these interesting effects, but also can reveal the symmetry restrictions in the system. Understanding the symmetry and how it changes is an effective tool when it comes to probing new phases of matter[33].

In the multiferroric $Sr_2FeSi_2O_7$, we effectively drew a link between the spin-orbit coupling (SOC) effect and the coupling of the two order parameters, magnetization $\mathbf{M}$ and electric polarization $\mathbf{P}$. It is well known that the SOC effect has an energy scale much smaller than the other dominant effects in 3d electronic systems, namely Hund's coupling (electronic exchange) and crystal field splitting. Our observations confirmed that through the 2nd order perturbation effect, SOC lifts the degeneracy of the Fe^{2+} ($3d^6$) electronic ground state. Our theoretical analysis and experimental results also confirms that the actual ground state is that of both spin and orbital in origin. Interestingly, the energetics of the single ion picture is the origin for the single ion anisotropy energy in the magnetic order phase. Since the electronic ground state of a single ion has no S_z, in the magnetically ordered phase, the spins structure is an easy-plane (xy) one. The required energy to take the spins out of this plane is closely related to the energy difference between our measured ground state and the first excited state.

In a different material, $CaFe_2O_4$, we measured the effect of crystalline symmetry on the antiferromagnetic magnons of the system. Below ≈ 200 K, this material order antiferromagnetically with the magnetic moments point parallel and antiparallel to the crystalline b-axis. Although the magnetic structure is complicated, a mean field theory that only takes into account the orthorhombic symmetry of the crystal lattice can qualitatively explain our observations. We observed two spin wave (magnon) modes with different energies. They are coming from the fact that the single ion anisotropy terms in the spin Hamiltonian has to reflect the highly anisotropic nature of this crystal. Interestingly, our THz spectroscopy probe manage to catch a glimpse of the coexistence of two magnetic phases in $CaFe_2O_4$. A better theoretical study is necessary to fully explain our observations.

In the last study presented here, we demonstrated that the normal modes of lattice vibration (phonons) are highly sensitive to the symmetry of the crystal. α-$RuCl_3$ belongs to the monoclinic crystal group, one of the lower symmetry crystal groups. Each van der Waals layer is a nearly perfect honeycomb. The symmetry breaking also comes from the monoclinic stacking, where the near perfect honeycomb layers are stacked at a low symmetry angle of $\sim 180°$. We observed the effect of these broken symmetries in the Raman phonon spectra. We have good evidence to show that each of the perfect honeycomb layer's E_g (doubly degenerate) phonons is split into pairs of A_g and B_g phonons. The subtle splitting can only be explained by either the weak van der Waals coupling or the distorted honeycomb layer. We also investigated the asymmetric phonon peak that's often associated with magnetic scattering in previous studies. Our analysis revealed that the scattering continuum is of the E_g symmetry, vanishing when the excitation fields are out of the honeycomb plane. Comparing to previously derived selection rules, we concluded that the observed scattering continuum at room temperature is possibly magnetic, and the magnetic interaction is that of only nearest neighbor and obeying the crystal symmetry.

These studies are some of the examples of how optical spectroscopy can probe the symmetry and symmetry breaking effects in solids. Many exotic phases of matter require highly sensitive optical probes due to their more subtle fingerprints. Performing spectroscopy in the infrared and far infrared range is a great way to probe the low-energy excitations of the

crystal or magnetic structure.

Bibliography

[1] Wikimedia Commons. Electromagnetic spectrum, 2019.

[2] D. N. Basov, Richard D. Averitt, Dirk van der Marel, Martin Dressel, and Kristjan Haule. Electrodynamics of correlated electron materials. *Rev. Mod. Phys.*, 83:471–541, Jun 2011.

[3] N. J. Laurita, J. Deisenhofer, LiDong Pan, C. M. Morris, M. Schmidt, M. Johnsson, V. Tsurkan, A. Loidl, and N. P. Armitage. Singlet-triplet excitations and long-range entanglement in the spin-orbital liquid candidate $fesc_2s_4$. *Phys. Rev. Lett.*, 114:207201, May 2015.

[4] Claudia Brückner, Gunther Notni, and Andreas Tünnermann. Optimal arrangement of 90° off-axis parabolic mirrors in thz setups. *Optik*, 121(1):113 – 119, 2010.

[5] Wikimedia Commons. Raman scattering, 2019.

[6] W. Low and M. Weger. Paramagnetic resonance and optical spectra of divalent iron in cubic fields. i. theory. *Phys. Rev.*, 118:1119–1130, Jun 1960.

[7] C. Stock, E. E. Rodriguez, N. Lee, M. A. Green, F. Demmel, R. A. Ewings, P. Fouquet, M. Laver, Ch. Niedermayer, Y. Su, K. Nemkovski, J. A. Rodriguez-Rivera, and S.-W. Cheong. Solitary magnons in the $s = \frac{5}{2}$ antiferromagnet $cafe_2o_4$. *Phys. Rev. Lett.*, 117:017201, Jun 2016.

[8] A. Glamazda, P. Lemmens, S.-H. Do, Y. S. Kwon, and K.-Y. Choi. Relation between kitaev magnetism and structure in $\alpha - rucl_3$. *Phys. Rev. B*, 95:174429, May 2017.

[9] Joseph D. Martin. When condensed-matter physics became king, Jan 2019.

[10] N.W. Ashcroft and N.D. Mermin. *Solid State Physics*. Cengage Learning, 2011.

[11] Robert W. Boyd. *Nonlinear Optics, Third Edition*. Academic Press, Inc., Orlando, FL, USA, 3rd edition, 2008.

[12] John David Jackson. *Classical Electrodynamics*. Wiley, 3rd ed. edition, 1999.

[13] D. H. Auston, K. P. Cheung, and P. R. Smith. Picosecond photoconducting hertzian dipoles. *Applied Physics Letters*, 45(3):284–286, 1984.

[14] P. R. Smith, D. H. Auston, and M. C. Nuss. Subpicosecond photoconducting dipole antennas. *IEEE Journal of Quantum Electronics*, 24(2):255–260, Feb 1988.

[15] D. Grischkowsky, Søren Keiding, Martin van Exter, and Ch. Fattinger. Far-infrared time-domain spectroscopy with terahertz beams of dielectrics and semiconductors. *J. Opt. Soc. Am. B*, 7(10):2006–2015, Oct 1990.

[16] P.U. Jepsen, D.G. Cooke, and M. Koch. Terahertz spectroscopy and imaging – modern techniques and applications. *Laser & Photonics Reviews*, 5(1):124–166, 2011.

[17] T. Seifert, S. Jaiswal, U. Martens, J. Hannegan, L. Braun, P. Maldonado, F. Freimuth, A. Kronenberg, J. Henrizi, I. Radu, E. Beaurepaire, Y. Mokrousov, P. M. Oppeneer, M. Jourdan, G. Jakob, D. Turchinovich, L. M. Hayden, M. Wolf, M. Münzenberg, M. Kläui, and T. Kampfrath. Efficient metallic spintronic emitters of ultrabroadband terahertz radiation. *Nature Photonics*, 10:483 EP –, May 2016. Article.

[18] Lucas S. Bilbro. *Fluctuations of Superconductivity in $La_{2-x}Sr_xCuO_4$ measured with Terahertz Time-Domain Spectroscopy*. Ph.d. dissertation, John Hopkins University, 2012.

[19] N. J. Laurita, Bing Cheng, R. Barkhouser, V. A. Neumann, and N. P. Armitage. A modified 8f geometry with reduced optical aberrations for improved time domain tera-

hertz spectroscopy. *Journal of Infrared, Millimeter, and Terahertz Waves*, 37(9):894–902, Sep 2016.

[20] Fabian D. J. Brunner, Arno Schneider, and Peter Günter. A terahertz time-domain spectrometer for simultaneous transmission and reflection measurements at normal incidence. *Opt. Express*, 17(23):20684–20693, Nov 2009.

[21] B. S. . Ung, J. Li, H. Lin, B. M. Fischer, W. Withayachumnankul, and D. Abbott. Dual-mode terahertz time-domain spectroscopy system. *IEEE Transactions on Terahertz Science and Technology*, 3(2):216–220, March 2013.

[22] R. S. Krishnan and R. K. Shankar. Raman effect: History of the discovery. *Journal of Raman Spectroscopy*, 10(1):1–8, 1981.

[23] Patrick J. Hendra and P. M. Stratton. Laser-raman spectroscopy. *Chemical Reviews*, 69(3):325–344, 1969.

[24] R.R. Birss. *Symmetry and magnetism*. Selected topics in solid state physics. North-Holland Pub. Co., 1964.

[25] A.P. Cracknell. *Magnetism in Crystalline Materials: Applications of the Theory of Groups of Cambiant Symmetry*. International series of monographs in natural philosophy. Elsevier Science Limited, 1975.

[26] M.S. Dresselhaus, G. Dresselhaus, and A. Jorio. *Group Theory: Application to the Physics of Condensed Matter*. Springer Berlin Heidelberg, 2007.

[27] F.A. Cotton. *Chemical Applications of Group Theory*. A Wiley-Interscience publication. Wiley India, 2003.

[28] S. Sugano, Y. Tanabe, and H. Kamimura. *Multiplets of transition-metal ions in crystals*. Pure and applied physics. Academic Press, 1970.

[29] L.D. Landau, E.M. Lifshitz, and L.P. Pitaevskii. *Electrodynamics of continuous media*. Elsevier, 2 edition, 1984.

[30] L.D. Landau and E.M. Lifshitz. *Statistical Physics*. Number v. 5. Elsevier Science, 2013.

[31] Lars Onsager. Reciprocal relations in irreversible processes. i. *Phys. Rev.*, 37:405–426, Feb 1931.

[32] Lars Onsager. Reciprocal relations in irreversible processes. ii. *Phys. Rev.*, 38:2265–2279, Dec 1931.

[33] Liuyan Zhao, Darius Torchinsky, John Harter, Alberto de la Torre, and David Hsieh. Second harmonic generation spectroscopy of hidden phases. pages 207 – 226, 2018.

[34] R. Shankar. *Principles of Quantum Mechanics*. Springer US, 2011.

[35] F. Keffer and C. Kittel. Theory of antiferromagnetic resonance. *Phys. Rev.*, 85:329–337, Jan 1952.

[36] T. Kimura, T. Goto, H. Shintani, K. Ishizaka, T. Arima, and Y. Tokura. Magnetic control of ferroelectric polarization. *Nature*, 426(6962):55–58, 2003.

[37] N. Hur, S. Park, P.A. Sharma, J.S. Ahn, S. Guha, and S.-W. Cheong. Electric polarization reversal and memory in a multiferroic material induced by magnetic fields. *Nature*, 429(6990):392–395, 2004.

[38] S-W. Cheong and M. Mostovoy. Multiferroics: a magnetic twist for ferroelectricity. *Nature Materials*, 6:13–20, 2007.

[39] R. Ramesh and Nicola A. Spaldin. Multiferroics: progress and prospects in thin films. *Nature Materials*, 6:21, Jan 2007. Review Article.

[40] Manfred Fiebig, Thomas Lottermoser, Dennis Meier, and Morgan Trassin. The evolution of multiferroics. *Nature Reviews Materials*, 1:16046, Jul 2016. Review Article.

[41] S. Bordacs, I. Kezsmarki, and et al. Chirality of matter shows up via spin excitations. *Nature Physics*, 8(10):734–738, 2012.

[42] I. Kezsmarki, N. Kida, H. Murakawa, S. Bordacs, Y. Onose, and Y. Tokura. Enhanced directional dichroism of terahertz light in resonance with magnetic excitations of the multiferroic $ba_2coge_2o_7$ oxide compound. *Phys. Rev. Lett.*, 106:057403, Feb 2011.

[43] R. Valdés Aguilar, M. Mostovoy, A. B. Sushkov, C. L. Zhang, Y. J. Choi, S-W. Cheong, and H. D. Drew. Origin of electromagnon excitations in multiferroic $rmno_3$. *Phys. Rev. Lett.*, 102:047203, Jan 2009.

[44] A. Pimenov, A.A. Mukhin, V.Yu. Ivanov, V.D. Travkin, A.M. Balbashov, and A. Loidl. Possible evidence for electromagnons in multiferroic manganites. *Nature Physics*, 2(2):97–100, 2006.

[45] Daniel Ish and Leon Balents. Theory of excitations and dielectric response at a spin-orbital quantum critical point. *Phys. Rev. B*, 92:094413, Sep 2015.

[46] I. A. Sergienko and E. Dagotto. Role of the dzyaloshinskii-moriya interaction in multiferroic perovskites. *Phys. Rev. B*, 73:094434, Mar 2006.

[47] Hosho Katsura, Naoto Nagaosa, and Alexander V. Balatsky. Spin current and magnetoelectric effect in noncollinear magnets. *Phys. Rev. Lett.*, 95:057205, Jul 2005.

[48] I. Dzyaloshinsky. A thermodynamic theory of weak ferromagnetism of antiferromagnetics. *Journal of Physics and Chemistry of Solids*, 4(4):241 – 255, 1958.

[49] Tôru Moriya. New mechanism of anisotropic superexchange interaction. *Phys. Rev. Lett.*, 4:228–230, Mar 1960.

[50] Tôru Moriya. Anisotropic superexchange interaction and weak ferromagnetism. *Phys. Rev.*, 120:91–98, Oct 1960.

[51] Hosho Katsura, Alexander V. Balatsky, and Naoto Nagaosa. Dynamical magnetoelectric coupling in helical magnets. *Phys. Rev. Lett.*, 98:027203, Jan 2007.

[52] A B Sushkov, M Mostovoy, R Valdés Aguilar, S-W Cheong, and H D Drew. Electro-

magnons in multiferroic rmn 2 o 5 compounds and their microscopic origin. *Journal of Physics: Condensed Matter*, 20(43):434210, 2008.

[53] Judit Romhányi, Miklós Lajkó, and Karlo Penc. Zero- and finite-temperature mean field study of magnetic field induced electric polarization in $ba_2coge_2o_7$: Effect of the antiferroelectric coupling. *Phys. Rev. B*, 84:224419, Dec 2011.

[54] M. Soda, M. Matsumoto, M. Månsson, S. Ohira-Kawamura, K. Nakajima, R. Shiina, and T. Masuda. Spin-nematic interaction in the multiferroic compound $ba_2coge_2o_7$. *Phys. Rev. Lett.*, 112:127205, Mar 2014.

[55] H. Murakawa, Y. Onose, S. Miyahara, N. Furukawa, and Y. Tokura. Ferroelectricity induced by spin-dependent metal-ligand hybridization in $ba_2coge_2\mathbf{o}_7$. *Phys. Rev. Lett.*, 105:137202, Sep 2010.

[56] K. Penc, J. Romhányi, T. Rõ om, U. Nagel, Á. Antal, T. Fehér, A. Jánossy, H. Engelkamp, H. Murakawa, Y. Tokura, D. Szaller, S. Bordács, and I. Kézsmárki. Spin-stretching modes in anisotropic magnets: Spin-wave excitations in the multiferroic $ba_2coge_2\mathbf{o}_7$. *Phys. Rev. Lett.*, 108:257203, Jun 2012.

[57] Shin Miyahara and Nobuo Furukawa. Theory of magnetoelectric resonance in two-dimensional s = 3/2 antiferromagnet ba2coge2o7 via spin-dependent metal-ligand hybridization mechanism. *Journal of the Physical Society of Japan*, 80(7):073708, 2011.

[58] Judit Romhányi and Karlo Penc. Multiboson spin-wave theory for $ba_2coge_2o_7$: A spin-3/2 easy-plane néel antiferromagnet with strong single-ion anisotropy. *Phys. Rev. B*, 86:174428, Nov 2012.

[59] Kunihiko Yamauchi, Paolo Barone, and Silvia Picozzi. Theoretical investigation of magnetoelectric effects in $ba_2coge_2o_7$. *Phys. Rev. B*, 84:165137, Oct 2011.

[60] Paolo Barone, Kunihiko Yamauchi, and Silvia Picozzi. Jahn-teller distortions as a novel source of multiferroicity. *Phys. Rev. B*, 92:014116, Jul 2015.

[61] T-H. Jang, 2016. Private Communication.

[62] C. M. Morris, R. Valdés Aguilar, A. Ghosh, S. M. Koohpayeh, J. Krizan, R. J. Cava, O. Tchernyshyov, T. M. McQueen, and N. P. Armitage. Hierarchy of bound states in the one-dimensional ferromagnetic ising chain conb$_2$o$_6$ investigated by high-resolution time-domain terahertz spectroscopy. *Phys. Rev. Lett.*, 112:137403, Apr 2014.

[63] LiDong Pan, Se Kwon Kim, A Ghosh, Christopher M Morris, Kate A Ross, Edwin Kermarrec, Bruce D Gaulin, SM Koohpayeh, Oleg Tchernyshyov, and NP Armitage. Low-energy electrodynamics of novel spin excitations in the quantum spin ice yb2ti2o7. *Nature communications*, 5, 2014.

[64] Glen A. Slack, S. Roberts, and Frank S. Ham. Far-infrared optical absorption of fe^{2+} in zns. *Phys. Rev.*, 155:170–177, Mar 1967.

[65] L. Mittelstädt, M. Schmidt, Zhe Wang, F. Mayr, V. Tsurkan, P. Lunkenheimer, D. Ish, L. Balents, J. Deisenhofer, and A. Loidl. Spin-orbiton and quantum criticality in fesc$_2$s$_4$. *Phys. Rev. B*, 91:125112, Mar 2015.

[66] Daniel Ish and Leon Balents. Theory of excitations and dielectric response at a spin-orbital quantum critical point. *Phys. Rev. B*, 92:094413, Sep 2015.

[67] To avoid confusion, the single electron orbitals are labeled with lower-case letters, i.e. d-orbitals, whereas the multi-electron ground term is labeled with the upper-case letter D.

[68] D.I. Khomskii. *Transition Metal Compounds*. Cambridge University Press, 2014.

[69] A. Abragam and B. Bleaney. *Electron Paramagnetic Resonance of Transition Ions*. OUP Oxford, 2012.

[70] Yasumichi. Matsumoto, Masaru. Omae, Kazuyoshi. Sugiyama, and Eiichi. Sato. New photocathode materials for hydrogen evolution: calcium iron oxide (cafe2o4) and strontium iron oxide (sr7fe10o22). *The Journal of Physical Chemistry*, 91(3):577–581, 1987.

[71] María Isabel Díez-García and Roberto Gómez. Investigating water splitting with cafe2o4 photocathodes by electrochemical impedance spectroscopy. *ACS Applied Materials & Interfaces*, 8(33):21387–21397, 2016. PMID: 27466695.

[72] B. F. Decker and J. S. Kasper. The structure of calcium ferrite. *Acta Crystallographica*, 10(4):332–337, Apr 1957.

[73] T. Yamanaka, A. Uchida, and Y. Nakamoto. Structural transition of post-spinel phases camn2o4, cafe2o4, and cati2o4 under high pressures up to 80 gpa. *American Mineralogist*, 93(11-12):1874, 2008.

[74] L. M. Corliss, J. M. Hastings, and W. Kunnmann. Magnetic phase equilibrium in chromium-substituted calcium ferrite. *Phys. Rev.*, 160:408–413, Aug 1967.

[75] Hiroshi Watanabe, Hiroshi Yamauchi, Masayoshi Ohashi, Mitsuo Sugimoto, Takuya Okada, and Masahiro Fukase. Neutron diffraction study of cafe2o4. *Journal of the Physical Society of Japan*, 22(3):939–939, 1967.

[76] C. Stock, E. E. Rodriguez, N. Lee, F. Demmel, P. Fouquet, M. Laver, Ch. Niedermayer, Y. Su, K. Nemkovski, M. A. Green, J. A. Rodriguez-Rivera, J. W. Kim, L. Zhang, and S.-W. Cheong. Orphan spins in the $s = \frac{5}{2}$ antiferromagnet cafe$_2$o$_4$. *Phys. Rev. Lett.*, 119:257204, Dec 2017.

[77] R. Coldea, D. A. Tennant, E. M. Wheeler, E. Wawrzynska, D. Prabhakaran, M. Telling, K. Habicht, P. Smeibidl, and K. Kiefer. Quantum criticality in an ising chain: Experimental evidence for emergent e8 symmetry. *Science*, 327(5962):177–180, 2010.

[78] C. M. Morris, R. Valdés Aguilar, A. Ghosh, S. M. Koohpayeh, J. Krizan, R. J. Cava, O. Tchernyshyov, T. M. McQueen, and N. P. Armitage. Hierarchy of bound states in the one-dimensional ferromagnetic ising chain conb$_2$o$_6$ investigated by high-resolution time-domain terahertz spectroscopy. *Phys. Rev. Lett.*, 112:137403, Apr 2014.

[79] Lucile Savary and Leon Balents. Quantum spin liquids: a review. *Reports on Progress in Physics*, 80(1):016502, nov 2016.

[80] Alexei Kitaev. Anyons in an exactly solved model and beyond". *Annals of Physics*, 321(1):2 – 111, 2006. January Special Issue.

[81] M. Hermanns, I. Kimchi, and J. Knolle. Physics of the kitaev model: Fractionalization, dynamic correlations, and material connections. *Annual Review of Condensed Matter Physics*, 9(1):17–33, 2018.

[82] H. B. Cao, A. Banerjee, J.-Q. Yan, C. A. Bridges, M. D. Lumsden, D. G. Mandrus, D. A. Tennant, B. C. Chakoumakos, and S. E. Nagler. Low-temperature crystal and magnetic structure of $\alpha - $rucl$_3$. *Phys. Rev. B*, 93:134423, Apr 2016.

[83] R. D. Johnson, S. C. Williams, A. A. Haghighirad, J. Singleton, V. Zapf, P. Manuel, I. I. Mazin, Y. Li, H. O. Jeschke, R. Valentí, and R. Coldea. Monoclinic crystal structure of $\alpha - $rucl$_3$ and the zigzag antiferromagnetic ground state. *Phys. Rev. B*, 92:235119, Dec 2015.

[84] Arnab Banerjee, Jiaqiang Yan, Johannes Knolle, Craig A. Bridges, Matthew B. Stone, Mark D. Lumsden, David G. Mandrus, David A. Tennant, Roderich Moessner, and Stephen E. Nagler. Neutron scattering in the proximate quantum spin liquid α-rucl3. *Science*, 356(6342):1055–1059, 2017.

[85] Arnab Banerjee, Paula Lampen-Kelley, Johannes Knolle, Christian Balz, Adam Anthony Aczel, Barry Winn, Yaohua Liu, Daniel Pajerowski, Jiaqiang Yan, Craig A. Bridges, Andrei T. Savici, Bryan C. Chakoumakos, Mark D. Lumsden, David Alan Tennant, Roderich Moessner, David G. Mandrus, and Stephen E. Nagler. Excitations in the field-induced quantum spin liquid state of a-rucl3. *npj Quantum Materials*, 3(1):8, 2018.

[86] A. Little, Liang Wu, P. Lampen-Kelley, A. Banerjee, S. Patankar, D. Rees, C. A. Bridges, J.-Q. Yan, D. Mandrus, S. E. Nagler, and J. Orenstein. Antiferromagnetic resonance and terahertz continuum in $\alpha-$rucl$_3$. *Phys. Rev. Lett.*, 119:227201, Nov 2017.

[87] Zhe Wang, S. Reschke, D. Hüvonen, S.-H. Do, K.-Y. Choi, M. Gensch, U. Nagel, T. Rõom, and A. Loidl. Magnetic excitations and continuum of a possibly field-induced quantum spin liquid in $\alpha-$rucl$_3$. *Phys. Rev. Lett.*, 119:227202, Nov 2017.

[88] Liang Wu, A. Little, E. E. Aldape, D. Rees, E. Thewalt, P. Lampen-Kelley, A. Banerjee, C. A. Bridges, J.-Q. Yan, D. Boone, S. Patankar, D. Goldhaber-Gordon, D. Mandrus, S. E. Nagler, E. Altman, and J. Orenstein. Field evolution of magnons in $\alpha-$rucl$_3$ by high-resolution polarized terahertz spectroscopy. *Phys. Rev. B*, 98:094425, Sep 2018.

[89] Luke J. Sandilands, Yao Tian, Kemp W. Plumb, Young-June Kim, and Kenneth S. Burch. Scattering continuum and possible fractionalized excitations in $\alpha-$rucl$_3$. *Phys. Rev. Lett.*, 114:147201, Apr 2015.

[90] Boyi Zhou, Yiping Wang, Gavin B. Osterhoudt, Paula Lampen-Kelley, David Mandrus, Rui He, Kenneth S. Burch, and Erik A. Henriksen. Possible structural transformation and enhanced magnetic fluctuations in exfoliated $\alpha-$rucl$_3$. *Journal of Physics and Chemistry of Solids*, 2018.

[91] J. Knolle, Gia-Wei Chern, D. L. Kovrizhin, R. Moessner, and N. B. Perkins. Raman scattering signatures of kitaev spin liquids in A_2iro$_3$ iridates with $a =$ Na or li. *Phys. Rev. Lett.*, 113:187201, Oct 2014.

[92] U. Fano. Effects of configuration interaction on intensities and phase shifts. *Phys. Rev.*, 124:1866–1878, Dec 1961.

[93] J. Nasu, J. Knolle, D. L. Kovrizhin, Y. Motome, and R. Moessner. Fermionic response from fractionalization in an insulating two-dimensional magnet. *Nature Physics*, 12:912, Jul 2016.

[94] A. Glamazda, P. Lemmens, S.-H. Do, Y. S. Choi, and K.-Y. Choi. Raman spectroscopic signature of fractionalized excitations in the harmonic-honeycomb iridates $\beta-and\gamma$-li2iro3. *Nature Communications*, 7:12286 EP –, Jul 2016.

[95] V. M. Bermudez. Unit-cell vibrational spectra of chromium trichoride and chromium tribromide. *Solid State Communications*, 19:693–697, Jul 1976.

[96] Daniel T. Larson and Efthimios Kaxiras. Raman spectrum of cri$_3$: An *ab initio* study. *Phys. Rev. B*, 98:085406, Aug 2018.

[97] Brent Perreault, Johannes Knolle, Natalia B. Perkins, and F. J. Burnell. Theory of raman response in three-dimensional kitaev spin liquids: Application to β- and $\gamma-$li$_2$iro$_3$ compounds. *Phys. Rev. B*, 92:094439, Sep 2015.